

1 SEARCH FOR $t\bar{t}Z' \rightarrow t\bar{t}t\bar{t}$ PRODUCTION IN THE MULTILEPTON FINAL STATE IN
2 pp COLLISIONS AT $\sqrt{s} = 13$ TEV WITH THE ATLAS DETECTOR

By

Hieu Le

A DISSERTATION

Submitted to
Michigan State University
in partial fulfillment of the requirements
for the degree of

Physics — Doctor of Philosophy

2025

ABSTRACT

13 Lorem ipsum dolor sit amet, consectetur adipiscing elit, sed do eiusmod tempor incididunt ut
14 labore et dolore magna aliqua. Ut enim ad minim veniam, quis nostrud exercitation ullamco
15 laboris nisi ut aliquip ex ea commodo consequat. Duis aute irure dolor in reprehenderit in
16 voluptate velit esse cillum dolore eu fugiat nulla pariatur. Excepteur sint occaecat cupidatat
17 non proident, sunt in culpa qui officia deserunt mollit anim id est laborum.

ACKNOWLEDGMENTS

- ¹⁹ Advisor: Reinhard Schwienhorst
- ²⁰ Postdoc: Binbin Dong
- ²¹ Committee
- ²² MSU group
- ²³ ATLAS analysis group
- ²⁴ Friend: Daniel, Grayson, Bella, Eric, Jordan
- ²⁵ Other friends: Jasper, Adam, Brittany
- ²⁶ Parents
- ²⁷ Spouse: Allen Sechrist
- ²⁸ ATLAS in general & funding agencies

PREFACE

³⁰ This is my preface. remarks remarks remarks

TABLE OF CONTENTS

31	List of Tables	vii
32	List of Figures	viii
33	KEY TO ABBREVIATIONS	ix
34	Roadmap	1
35	Chapter 1. Introduction	2
36	Chapter 2. Theoretical Overview	3
37	2.1 The Standard Model	3
38	2.1.1 Elementary particles	3
39	2.1.2 Mathematical formalism	7
40	2.1.2.1 Quantum chromodynamics	8
41	2.1.2.2 Electroweak theory	10
42	2.1.2.3 Higgs mechanism	13
43	2.2 Beyond the Standard Model	16
44	2.2.1 Top-philic vector resonance	16
45	2.2.2 BSM four-top quark production	19
46	Chapter 3. LHC & ATLAS Experiment	21
47	3.1 The Large Hadron Collider	21
48	3.1.1 Overview	21
49	3.1.2 LHC operations	21
50	3.2 The ATLAS detector	24
51	3.2.1 Inner detector	24
52	3.2.2 Calorimeter systems	26
53	3.2.3 Muon spectrometer	27
54	3.2.4 Forward detectors	29
55	3.2.5 Magnetic systems	29
56	3.2.6 Trigger & data acquisition	30
57	Chapter 4. Particle Reconstruction & Identification	32
58	4.1 Primary reconstruction	32
59	4.1.1 Topological clusters	32
60	4.1.2 Tracks	33
61	4.1.3 Vertices	34
62	4.2 Jets	35
63	4.2.1 Flavor tagging	36
64	4.3 Leptons	39
65	4.3.1 Electrons	39

66	4.3.2 Muons	42
67	4.4 Missing transverse momentum	44
68	4.5 Overlap removal	46
69	4.6 Object definition	46
70	Chapter 5. Data & Simulated Samples	48
71	5.1 Data samples	48
72	5.2 Monte Carlo samples	49
73	5.2.1 $t\bar{t}Z'$ signal samples	49
74	5.2.2 Background samples	49
75	Chapter 6. Analysis Strategy	51
76	6.1 Event selection	51
77	6.2 Analysis regions	53
78	6.2.1 Signal regions	53
79	6.2.2 Control regions	54
80	6.2.3 Validation regions	56
81	6.3 Background estimation	58
82	6.3.1 Template fitting for fake/non-prompt estimation	58
83	6.3.2 Charge misidentification data-driven estimation	59
84	6.3.3 $t\bar{t}W$ background data-driven estimation	61
85	Chapter 7. Systematic Uncertainties	65
86	7.1 Experimental uncertainties	65
87	7.1.1 Leptons	65
88	7.1.2 Jets	66
89	7.1.3 Missing transverse energy	68
90	7.2 Modeling uncertainties	68
91	7.2.1 Signal and irreducible background uncertainties	68
92	7.2.2 Reducible background uncertainties	71
93	Chapter 8. Results	74
94	8.1 Statistical model	74
95	8.1.1 Binned profile likelihood fit	74
96	8.1.2 Signal significance	74
97	8.1.3 Limit exclusion	74
98	8.2 Fit results	74
99	8.3 Limits	75
100	Chapter 9. Summary	76
101	References	77

¹⁰² List of Tables

¹⁰³ Table 4.1: Caption	46
¹⁰⁴ Table 4.2: Caption	47
¹⁰⁵ Table 5.1: Caption	48
¹⁰⁶ Table 5.2: Summary of all Monte-Carlo samples used in this analysis.	50
¹⁰⁷ Table 6.1: Caption	54
¹⁰⁸ Table 6.2: Caption	55
¹⁰⁹ Table 6.3: Caption	57
¹¹⁰ Table 7.1: Summary of the experimental systematic uncertainties considered in this ¹¹¹ analysis.	69
¹¹² Table 7.2: Caption	72
¹¹³ Table 7.3: Caption	73

¹¹⁴ List of Figures

¹¹⁵ Figure 2.1: Caption	4
¹¹⁶ Figure 2.2: Caption	7
¹¹⁷ Figure 2.3: Caption	18
¹¹⁸ Figure 2.4: Caption	20
¹¹⁹ Figure 3.1: Caption	22
¹²⁰ Figure 3.2: Caption	23
¹²¹ Figure 3.3: Caption	26
¹²² Figure 4.1:	33
¹²³ Figure 4.2: Caption	38

KEY TO ABBREVIATIONS

Physical & mathematical quantities

₁₂₆ χ^2 chi-squared

₁₂₇ ΔR angular distance

₁₂₈ η pseudorapidity

₁₂₉ E_T transverse energy

₁₃₀ E_T^{miss} missing transverse momentum

₁₃₁ γ_μ Dirac matrices

₁₃₂ I weak isospin

₁₃₃ L instantaneous luminosity

₁₃₄ μ signal strength

₁₃₅ p_T transverse momentum

Particles

₁₃₆ b bottom quark

₁₃₈ pp proton-proton

₁₃₉ $t\bar{t}$ top/anti-top quark

₁₄₀ $t\bar{t}t\bar{t}$ four-top-quark

₁₄₁ tW single-top

Acronyms

₁₄₂ **1LOS** one lepton, or two leptons of opposite charges

₁₄₄ **2HDM** two-Higgs doublet model

₁₄₅ **AF3** AtlFast3 fast simulation

₁₄₆ **ATLAS** A Toroidal LHC ApparatuS

₁₄₇ **BDT** boosted decision tree

₁₄₈ **BSM** Beyond the Standard Model

- ₁₄₉ **CERN** European Organization for Nuclear Research
- ₁₅₀ **CMS** Compact Muon Solenoid
- ₁₅₁ **CR** control region
- ₁₅₂ **ECIDS** Electron Charge ID Selector
- ₁₅₃ **EM** electromagnetic
- ₁₅₄ **EW** electroweak
- ₁₅₅ **FS** full detector simulation
- ₁₅₆ **GNN** graph neural network
- ₁₅₇ **GUT** Grand Unified Theory
- ₁₅₈ **HLT** High-Level Trigger
- ₁₅₉ **ID** inner detector
- ₁₆₀ **JER** jet energy resolution
- ₁₆₁ **JES** jet energy scale
- ₁₆₂ **JVT** Jet Vertex Tagger
- ₁₆₃ **L1** Level 1
- ₁₆₄ **LH** likelihood
- ₁₆₅ **LLH** log-likelihood
- ₁₆₆ **LO** leading order
- ₁₆₇ **LAr** liquid argon
- ₁₆₈ **LHC** Large Hadron Collider
- ₁₆₉ **MET** missing transverse energy
- ₁₇₀ **NF** normalization factor
- ₁₇₁ **NLO** next-to-leading order
- ₁₇₂ **NNLO** next-to-next-to-leading order
- ₁₇₃ **NP** nuisance parameter
- ₁₇₄ **OP** operating point
- ₁₇₅ **PS** parton shower

- ₁₇₆ **PDF** parton distribution function
- ₁₇₇ **PCBT** pseudo-continuous b -tagging
- ₁₇₈ **QED** quantum electrodynamics
- ₁₇₉ **QCD** quantum chromodynamics
- ₁₈₀ **QFT** quantum field theory
- ₁₈₁ **QmisID** charge mis-identification
- ₁₈₂ **SF** scale factor
- ₁₈₃ **SM** Standard Model
- ₁₈₄ **SR** signal region
- ₁₈₅ **SSML** two leptons of the same charge, or more than two leptons (multilepton)
- ₁₈₆ **TDAQ** Trigger and Data Acquisiton
- ₁₈₇ **VEV** vacuum expectation value

¹⁸⁸ **Roadmap**

¹⁸⁹	1. Finish adding bullets for all sections	06/04
¹⁹⁰	Remaining	
¹⁹¹	• introduction	
¹⁹²	2. Fill in details	06/13
¹⁹³	• Add missing figures	
¹⁹⁴	• Add missing bib	
¹⁹⁵	3. Finalize analysis	
¹⁹⁶	4. String everything together	
¹⁹⁷	5. Miscellaneous/logistics (proofreading, review, ATLAS approval, etc.)	
¹⁹⁸	6. Submission to the graduate school	07/01
¹⁹⁹	7. Defense	07/15

200 **Chapter 1. Introduction**

201 1. background and context

202 2. problem to be solved in thesis

203 3. aim of analysis: Z' consequences of many BSM theories, searching for Z'

204 4. hypothesis/research question: searching for Z' in $t\bar{t}t\bar{t}$ SSML channel

205 5. methodology: data collection - ζ , analysis regions - ζ , binned likelihood fit

206 6. thesis structure:

207 • ch2: SM/BSM theoretical background

208 • ch3: LHC/ATLAS experiment

209 • ch4: samples used in the analysis

210 • ch5: ATLAS particle reconstruction and identification techniques, and object
211 definitions for the analysis

212 • ch6: analysis strategy

213 • ch7: systematic uncertainties affecting the analysis

214 • ch8: final results

215 • ch9: summary

216 **Chapter 2. Theoretical Overview**

217 **2.1 The Standard Model**

- 218 The Standard Model of Physics (SM) is currently the most successful formalism to describe
- 219 the physical world at a microscopic scale.
- 220 The SM provides descriptions for all currently known elementary particles and three out of
- 221 four fundamental forces with the exception of gravity.

222

223 **2.1.1 Elementary particles**

- 224 Elementary particles in the SM can be classified into two groups: bosons, consisting of particles following Bose-Einstein statistics with integer spin and fermions, consisting of particles following Fermi-Dirac statistics with half-integer spin
- 225
- 226
- 227 Fermions are the building blocks of composite particles and consequently all known matter,
- 228 and can be further split into quarks & leptons.
- 229 Bosons act as force mediators for all fundamental forces described by the SM. Bosons have
- 230 two types: a scalar boson with spin 0 and vector gauge bosons with spin 1.
- 231 For each elementary particle there also exists a corresponding antiparticle with identical
- 232 mass and opposite charge (electric or color).

233 **Fermions**

- 234 Quarks and leptons each has six flavors, grouped into three generations of doublets.
- 235 The six quark flavors consist of up (u), down (d), charm (c), strange (s), bottom (b) and top

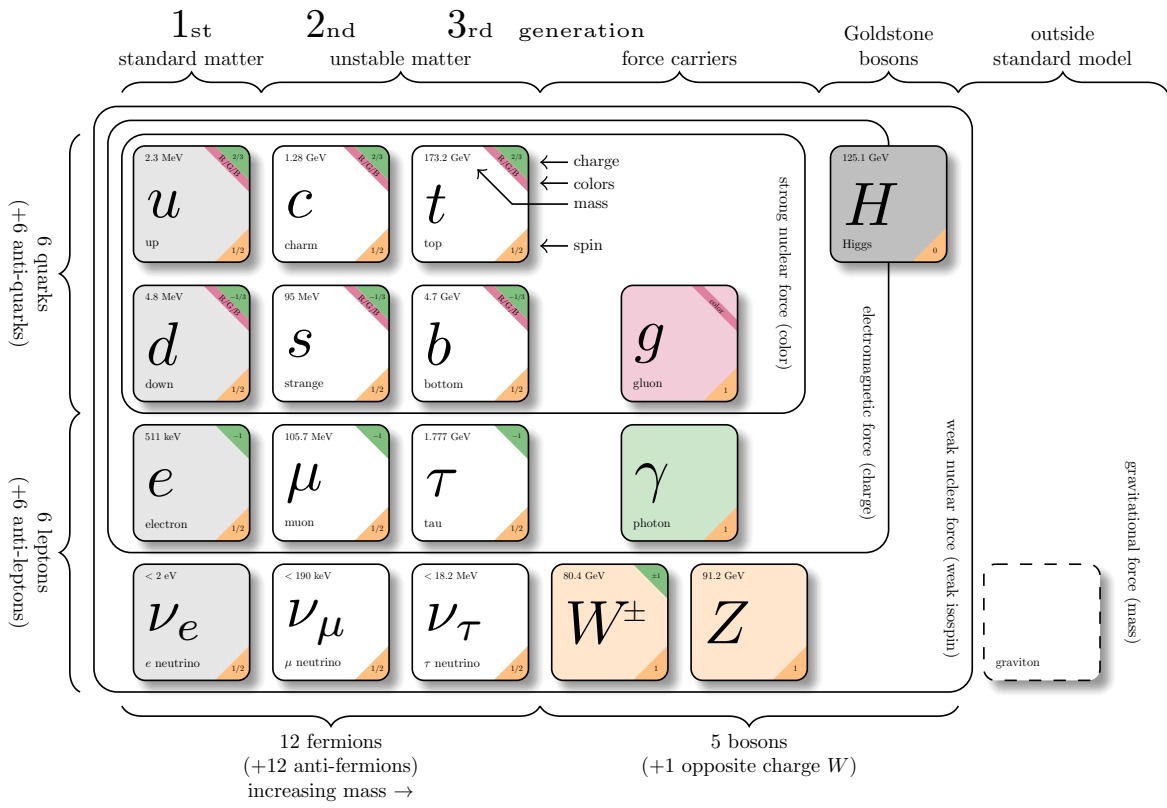


Figure 2.1: Caption[1]

²³⁶ (t) quark flavors in increasing order of mass, forming three doublets (u, d), (c, s) and (t, b).
²³⁷ Each doublet consists of one quark with electric charge of $+2/3$ (u, s, t), and one with charge
²³⁸ of $-1/3$ (d, c, b).
²³⁹ Each quark also has a property known as color charge, with possible values of red (R), green
²⁴⁰ (G), blue (B) or antired (\bar{R}), antigreen (\bar{G}), and antiblue (\bar{B}). Color charge follows color
²⁴¹ confinement rules, which allows only configurations of quarks with neutral color charge to
²⁴² exist in isolation. Neutral charge configurations can be formed from either a set of three
²⁴³ colors (R, G, B), a set of a color and its anticolor (q, \bar{q}), or any combination of the two.
²⁴⁴ Consequently, no isolated quark can exist in a vacuum and can only exist in bound states
²⁴⁵ called hadrons.
²⁴⁶ Quarks are the only elementary particles in the SM that can interact with all four funda-
²⁴⁷ mental forces.
²⁴⁸ The three leptons doublets consist of electron (e), muon (μ), tau (τ) and their respective
²⁴⁹ neutrino flavors: electron neutrino (ν_e), muon neutrino (ν_μ) and tau neutrino (ν_τ)
²⁵⁰ Charged leptons (e, μ, τ) carry an electric charge of -1 , while their antiparticles carry the
²⁵¹ opposite charge $+1$ and their corresponding neutrino flavors carrying no charge (charge neu-
²⁵² tral).
²⁵³ Charged leptons interact with all fundamental forces except the strong force, while neutrinos
²⁵⁴ only interact with the weak force and gravity.

²⁵⁵ **Bosons**

²⁵⁶ The SM classify bosons into two types: one scalar boson with spin 0 known as the Higgs
²⁵⁷ (H) boson, and vector gauge bosons with spin 1 known as gluons (g), photon (γ), W^\pm and
²⁵⁸ Z bosons.

- 259 The gluons and photon are massless, while the W^\pm , Z and H are massive.
- 260 Each vector gauge boson serves as the mediator for a fundamental force described by the
- 261 SM.
- 262 Gluons are massless mediator particles for the strong interaction between quarks according
- 263 to quantum chromodynamics (QCD), and carry the color charge in a strong interaction.
- 264 Each gluon carries a non-neutral color charge out of eight linearly independent color states
- 265 in the gluon color octet.
- 266 Photon is the massless and charge-neutral mediator particle for the electromagnetic interac-
- 267 tion following quantum electrodynamics (QED).
- 268 The W^\pm and Z bosons are massive mediator particles for the weak interaction, with the
- 269 W^\pm boson carrying an electric charge of ± 1 while the Z boson is charge neutral.
- 270 Other than the vector gauge boson, the only scalar boson in the SM is the Higgs boson which
- 271 is massive with electric charge of 0.
- 272 The Higgs boson does not mediate a fundamental force like vector bosons, but serve to
- 273 provide the rest mass for all massive elementary particles in the SM through the Higgs
- 274 mechanism as described in Section 2.21refsec:higgs.

275 Top quark

- 276 As of now, the top quark t is the heaviest particle in the SM with mass of about 173 GeV,
- 277 compared to the heaviest fermion, the Higgs boson at 125 GeV and the second most massive
- 278 fermion, the b -quark at about 4.2 GeV. This also gives it the strongest coupling to the Higgs
- 279 boson and exotic resonances in various proposed BSM models ([citations](#)), making the top
- 280 quark and its processes attractive vehicles with which to probe new physics.
- 281 Due to its mass, the top quark has a very short lifetime of 10^{-24} s, and consequently decays

before it can hadronize. The top quark decays to a W boson and a b -quark with a branching ratio of almost 100%, and is assumed to be such for the purpose of this analysis. The W boson can subsequently decay hadronically or leptonically as shown in Figure 2.2, with branching ratios of approximately 68% and 32% respectively and with all lepton flavors having similar ratios assuming lepton universality.

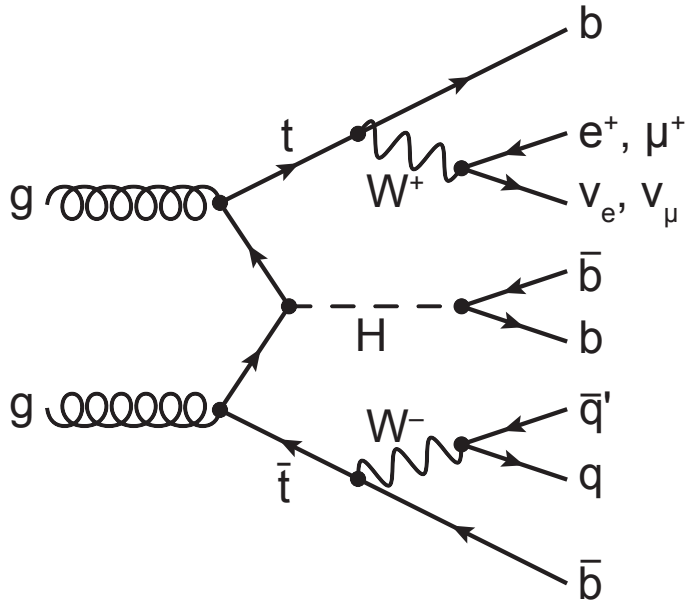


Figure 2.2: $H \rightarrow t\bar{t}$ possible, $t\bar{t}t\bar{t}$ final state[theory:ttH.Hbb]

2.1.2 Mathematical formalism

The SM can be described within the formalism of quantum field theory (QFT) with the Lagrangian

$$\mathcal{L}_{\text{SM}} = \mathcal{L}_{\text{QCD}} + \underbrace{(\mathcal{L}_{\text{gauge}} + \mathcal{L}_{\text{fermion}} + \mathcal{L}_{\text{Higgs}} + \mathcal{L}_{\text{Yukawa}})}_{\mathcal{L}_{\text{EW}}} \quad (2.1)$$

where \mathcal{L}_{QCD} is the QCD term and \mathcal{L}_{EW} is the electroweak (EW) term of the Lagrangian. QFT treats particles as excitations of their corresponding quantum fields: fermion field ψ ,

292 electroweak boson fields $W_{1,2,3}$ & B , gluon field G_α and Higgs field ϕ .

293 QFT depends heavily on gauge theory. A quantum field has gauge symmetry if there exists
294 a continuous gauge transformation that when applied to every point (local gauge transfor-
295 mation) leaves the field Lagrangian unchanged. The set of gauge transformations of a gauge
296 symmetry is the symmetry group of the field, which comes with a set of generators, each with
297 a corresponding gauge field. Under QFT, the quanta of these gauge fields are called gauge
298 bosons. The SM Lagrangian is gauge invariant under global Poincaré symmetry and local
299 $SU(3)_C \times SU(2)_L \times U(1)_Y$ gauge symmetry, with the gauge term $SU(3)_C$ corresponding to
300 the strong interaction and $SU(2)_L \times U(1)_Y$ to the EW interaction.

301 Global Poincaré symmetry ensures that \mathcal{L}_{SM} satisfies translational symmetry, rotational
302 symmetry and Lorentz boost frame invariance. By Noether's theorem, gauge symmetries
303 lead to corresponding conservation laws which leads to conservation of momentum, angular
304 momentum and energy in the SM.

305 2.1.2.1 Quantum chromodynamics

306 QCD is a non-Abelian gauge theory (Yang-Mills theory) describing the strong interaction
307 between quarks in the SM with the gauge group $SU(3)_C$, where C represents conservation
308 of color charge under $SU(3)_C$ symmetry.

309 According to QFT, quarks can be treated as excitations of corresponding quark fields ψ .
310 Quark fields are invariant under $SU(3)_C$ transformation

$$\psi \rightarrow e^{i\theta(x)T_a}\psi \quad (2.2)$$

₃₁₁ where T_a are generators of $SU(3)_C$, represented as $T_a = \lambda_a/2$ with λ_a being the eight Gell-
₃₁₂ Mann matrices.

₃₁₃ The free Dirac Lagrangian

$$\mathcal{L}_0 = \bar{\psi}(i\gamma^\mu \partial_\mu - m)\psi \quad (2.3)$$

₃₁₄ is invariant under global $SU(3)$ symmetry, but not under local $SU(3)_C$ symmetry. To
₃₁₅ establish invariance under local $SU(3)_C$ symmetry, the gauge covariant derivative D_μ is
₃₁₆ defined so that

$$D_\mu \psi = (\partial_\mu - ig_s G_\mu^a T_a) \psi, \quad (2.4)$$

₃₁₇ where $g_s = \sqrt{4\pi\alpha_s}$ is the QCD coupling constant, $G_\mu^a(x)$ are the eight gluon fields that
₃₁₈ transform under $SU(3)_C$ as

$$G_\mu^a \rightarrow e^{iT_a \theta_a(x)} \left(G_\mu^a + \frac{i}{g_s} \partial_\mu \right) e^{-iT_a \theta_a(x)} = G_\mu^a - \frac{1}{g_s} \partial_\mu \theta_a(x) - f_{abc} \theta_b(x) G_\mu^c, \quad (2.5)$$

₃₁₉ and T_a are the generators of $SU(3)_C$ defined as $T_a = \lambda_a/2$ with λ_a being the eight Gell-Mann
₃₂₀ matrices.

₃₂₁ Defining the gluon field strength tensor $G_{\mu\nu}^a$ as

$$G_{\mu\nu}^a \equiv \partial_\mu G_\nu^a - \partial_\nu G_\mu^a - g_s f^{abc} G_\mu^b G_\nu^c, \quad (2.6)$$

₃₂₂ where f^{abc} are the structure constants of $SU(3)_C$, the gauge invariant QCD Lagrangian is

$$\mathcal{L}_{\text{QCD}} = \bar{\psi}(i\gamma^\mu D_\mu - m)\psi - \frac{1}{4} G_{\mu\nu}^a G_a^{\mu\nu}, \quad (2.7)$$

³²³ which can be expressed in the form of

$$\mathcal{L}_{\text{QCD}} = \underbrace{-\frac{1}{4}G_{\mu\nu}^a G_a^{\mu\nu}}_{\text{gluon kinematics}} + \underbrace{\bar{\psi}(i\gamma^\mu \partial_\mu - m)\psi}_{\text{quark kinematics}} + \underbrace{\bar{\psi}^i(g_s \gamma^\mu (T_a)_{ij} G_\mu^a) \bar{\psi}^j}_{\text{quark-gluon interaction}}. \quad (2.8)$$

³²⁴ with i, j being the color indices with integer values from 1 to 3. The noncommutativity
³²⁵ of $SU(3)_C$ gives rise to an additional term consisting of only gluon fields and gluon-gluon
³²⁶ interactions. Additionally, the Lagrangian also forces gluons to be massless to maintain
³²⁷ gauge invariance.

³²⁸ 2.1.2.2 Electroweak theory

³²⁹ The electroweak interaction is the unified description of the weak interaction and electro-
³³⁰ magnetism under the $SU(2)_L \times U(1)_Y$ symmetry group, where L represents the left-handed
³³¹ chirality of the weak interaction and Y represents the weak hypercharge quantum number.

³³² The quantum number associated with the weak chirality is the weak isospin I . The EW
³³³ quantum numbers are connected by the Gell-Mann-Nishijima relation

$$Q = I_3 + Y/2 \quad (2.9)$$

³³⁴ where Q is the electric charge and I_3 is the third component of weak isospin I .

³³⁵ Fermions can have either left-handed or right-handed chirality, and can be divided into
³³⁶ left-handed doublets and right-handed singlets

$$\psi_L = \begin{pmatrix} \nu_e \\ e_L \end{pmatrix}, \begin{pmatrix} \nu_\mu \\ \mu_L \end{pmatrix}, \begin{pmatrix} \nu_\tau \\ \tau_L \end{pmatrix}, \begin{pmatrix} u_L \\ d_L \end{pmatrix}, \begin{pmatrix} c_L \\ s_L \end{pmatrix}, \begin{pmatrix} t_L \\ b_L \end{pmatrix} \quad (2.10)$$

$$\psi_R = e_R, \mu_R, \tau_R, u_R, d_R, c_R, s_R, t_R, b_R,$$

³³⁷ with the exception of neutrino which can only have left-handed chirality in the SM.

³³⁸ Both left-handed and right-handed fermion fields are invariant under $U(1)_Y$ transformation

$$\psi \rightarrow e^{iY\theta(x)/2}\psi. \quad (2.11)$$

³³⁹ Similar to QCD, to establish invariance under local $U(1)_Y$ symmetry, the $U(1)_Y$ gauge

³⁴⁰ covariant derivative D_μ is defined as

$$D_\mu\phi = \left(\partial_\mu - ig'\frac{Y}{2}B_\mu\right)\psi \quad (2.12)$$

³⁴¹ where $B_\mu(x)$ is a vector gauge field that transforms under $U(1)_Y$ as

$$B_\mu \rightarrow B_\mu + \frac{1}{g'}\partial_\mu\theta(x) \quad (2.13)$$

³⁴² and g' is the B_μ coupling constant.

³⁴³ Right-handed fermion singlets are not affected by $SU(2)_L$ transformation, so fermion fields

³⁴⁴ transform under $SU(2)_L$ as

$$\begin{aligned} \psi_L &\rightarrow e^{iI_3\vec{\theta}(x)\cdot\vec{\sigma}/2}\psi_L \\ \psi_R &\rightarrow \psi_R. \end{aligned} \quad (2.14)$$

³⁴⁵ where $\vec{\sigma}/2$ are generators of $SU(2)_L$ and $\vec{\sigma}$ are Pauli matrices. In order to preserve local

³⁴⁶ symmetry, the gauge covariant derivative for $SU(2)_L$ is defined as

$$D_\mu\psi_L = \left(\partial_\mu - ig\frac{\sigma_i}{2}W_\mu^i\right)\psi_L \quad (2.15)$$

³⁴⁷ where $W_\mu^i(x)$ ($i = 1, 2, 3$) are three boson gauge fields that transform under $SU(2)_L$ as

$$W_\mu^i \rightarrow e^{i\frac{\sigma_i}{2}\theta_i(x)} \left(W_\mu^i + \frac{i}{g}\partial_\mu \right) e^{-i\frac{\sigma_i}{2}\theta_i(x)} = W_\mu^i + \frac{2}{g}\partial_\mu\theta_a(x) + \epsilon^{ijk}\theta_j(x)W_\mu^k, \quad (2.16)$$

³⁴⁸ with g as the gauge coupling constant for W_μ^i , and ϵ^{ijk} as the structure constant for $SU(2)_L$.

³⁴⁹ The gauge covariant derivative for $SU(2)_L \times U(1)_Y$ can then be written as

$$\begin{aligned} D_\mu\psi_L &= \left(\partial_\mu - ig'\frac{Y_L}{2}B_\mu - ig\frac{\sigma_i}{2}W_\mu^i \right) \psi_L \\ D_\mu\psi_R &= \left(\partial_\mu - ig'\frac{Y_R}{2}B_\mu \right) \psi_R. \end{aligned} \quad (2.17)$$

³⁵⁰ Similar to QCD, the kinetic term is added by defining field strengths for the four gauge fields

$$\begin{aligned} B_{\mu\nu} &\equiv \partial_\mu B_\nu - \partial_\nu B_\mu \\ W_{\mu\nu}^i &\equiv \partial_\mu W_\nu^i - \partial_\nu W_\mu^i - ge^{ijk}W_\mu^jW_\nu^k. \end{aligned} \quad (2.18)$$

³⁵¹ The local $SU(2)_L \times U(1)_Y$ invariant EW Lagrangian can then be expressed as

$$\begin{aligned} \mathcal{L}_{\text{EW}} &= i\bar{\psi}(\gamma^\mu D_\mu)\psi - \frac{1}{4}W_{\mu\nu}^iW_i^{\mu\nu} - \frac{1}{4}B_{\mu\nu}B^{\mu\nu} \\ &= \underbrace{i\bar{\psi}(\gamma^\mu\partial_\mu)\psi}_{\text{fermion kinematics}} - \underbrace{\bar{\psi}\left(\gamma^\mu g'\frac{Y}{2}B_\mu\right)\psi}_{\text{fermion-gauge boson interaction}} - \underbrace{\bar{\psi}_L\left(\gamma^\mu g\frac{\sigma_i}{2}W_\mu^i\right)\psi_L}_{\text{boson kinematics \& self-interaction}} - \frac{1}{4}W_{\mu\nu}^iW_i^{\mu\nu} - \frac{1}{4}B_{\mu\nu}B^{\mu\nu}. \end{aligned} \quad (2.19)$$

³⁵² Under ≈ 159.5 GeV, the EW symmetry $SU(2)_L \times U(1)_Y$ undergoes spontaneous symme-

³⁵³ try breaking into $U(1)_{\text{QED}}$ symmetry, which corresponds to a separation of the weak and

³⁵⁴ electrodynamic forces. This replaces the massless and similarly-behaved EW gauge bosons

³⁵⁵ B_μ and W_μ^i with the EM boson γ and the weak bosons Z/W^\pm . Additionally, electroweak

³⁵⁶ spontaneous symmetry breaking also gives Z and W^\pm masses via the Higgs mechanism, dis-

³⁵⁷ cussed in Section 2.1.2.3. The spontaneous symmetry breaking leads to reparameterization
³⁵⁸ of B_μ and W_μ^i to $W^\pm/Z/\gamma$ bosons via a specific choice of gauge for the Higgs field

$$W_\mu^\pm \equiv \frac{1}{\sqrt{2}} (W_\mu^1 \mp i W_\mu^2)$$

$$\begin{pmatrix} A_\mu \\ Z_\mu \end{pmatrix} \equiv \begin{pmatrix} \cos \theta_W & \sin \theta_W \\ -\sin \theta_W & \cos \theta_W \end{pmatrix} \begin{pmatrix} B_\mu \\ W_\mu^3 \end{pmatrix} \quad (2.20)$$

³⁵⁹ where $\theta_W \equiv \cos^{-1} (g/\sqrt{g^2 + g'^2})$ is the weak mixing angle. The boson kinetic term can also
³⁶⁰ be refactorized to extract cubic (three vertices) and quartic (four vertices) self-interactions
³⁶¹ among the gauge bosons [2]. The Lagrangian can then be rewritten as

$$\mathcal{L} = \underbrace{eA_\mu \bar{\psi} (\gamma^\mu Q) \psi}_{\text{electromagnetism}} + \underbrace{\frac{e}{2\sin \theta_W \cos \theta_W} \bar{\psi} \gamma^\mu (v_f - a_f \gamma_5) \psi Z_\mu}_{\text{neutral current interaction}}$$

$$+ \underbrace{\frac{g}{2\sqrt{2}} \sum_{\psi_L} [\bar{f}_2 \gamma^\mu (1 - \gamma_5) f_1 W_\mu^+ + \bar{f}_1 \gamma^\mu (1 - \gamma_5) f_2 W_\mu^-]}_{\text{charged current interaction}} \quad (2.21)$$

$$+ \mathcal{L}_{\text{kinetic}} + \underbrace{\mathcal{L}_{\text{cubic}} + \mathcal{L}_{\text{quartic}}}_{\text{boson self-interaction}}$$

³⁶² where $\gamma_5 = i\gamma^0\gamma^1\gamma^2\gamma^3$ is the chirality projection operator, $a_f = I_3$, $v_f = I_3(1 - 4|Q|\sin^2 \theta_W)$
³⁶³ and f_1, f_2 are up and down type fermions of a left-handed doublet.

³⁶⁴ 2.1.2.3 Higgs mechanism

³⁶⁵ So far, the EW bosons are massless, since the mass terms $-m\bar{\psi}\psi$ for fermions and $-mA^\mu A_\mu$
³⁶⁶ for bosons are not invariant under the EW Lagrangian. The particles must then acquire
³⁶⁷ mass under another mechanism. The Brout-Engler-Higgs mechanism [3–5] was introduced

³⁶⁸ in 1964 to rectify this issue, and verified in 2012 with the discovery of the Higgs boson [6, 7].

³⁶⁹ The Higgs potential is expressed as

$$V(\phi^\dagger \phi) = \mu^2 \phi^\dagger \phi + \lambda (\phi^\dagger \phi)^2 \quad (2.22)$$

³⁷⁰ where μ^2 and $\lambda > 0$ are arbitrary parameters, and the $SU(2)_L$ doublet ϕ is the Higgs field

$$\phi = \begin{pmatrix} \phi^+ \\ \phi^0 \end{pmatrix}, \quad (2.23)$$

³⁷¹ with complex scalar fields ϕ^+ and ϕ^0 carrying +1 and 0 electric charge respectively. The

³⁷² Lagrangian for a scalar field is

$$\mathcal{L}_H = (\partial_\mu \phi)^\dagger (\partial^\mu \phi) - V(\phi^\dagger \phi). \quad (2.24)$$

³⁷³ Since the potential $V(\phi^\dagger \phi)$ is constrained by $\lambda > 0$, the ground state is solely controlled by

³⁷⁴ μ . If $\mu^2 > 0$, the ground state would be $\phi = 0$, and the EW bosons would remain massless.

³⁷⁵ If $\mu^2 < 0$, the ground state would be

$$|\phi|^2 = -\frac{\mu^2}{2\lambda} \equiv \frac{v^2}{\sqrt{2}}, \quad (2.25)$$

³⁷⁶ where v is defined as the vacuum expectation value (VEV). The standard ground state for

³⁷⁷ the Higgs potential without loss of generality can be chosen as

$$\phi(0) = \frac{1}{\sqrt{2}} \begin{pmatrix} 0 \\ v \end{pmatrix}. \quad (2.26)$$

sombrero potential pic

Having $U(1)$ symmetry allows any $-e^{i\theta}\sqrt{\mu^2/\lambda}$ to be a ground state energy for the Higgs Lagrangian. This degeneracy results in spontaneous symmetry breaking of the $SU(2)_L \times U(1)_Y$ symmetry into $U(1)_{\text{QED}}$ symmetry when the Higgs field settles on a specific vacuum state as a result of a perturbation or excitation. The spontaneous symmetry breaking introduces three massless (Nambu-Goldstone) vector gauge boson ξ and a massive scalar boson η , each corresponds to a generator of the gauge group. The bosons can be extracted using the reparameterization [8]

$$\xi \equiv \phi^+ \sqrt{2}, \quad \eta \equiv \phi^0 \sqrt{2} - v, \quad (2.27)$$

³⁷⁸ such that ξ, η are real fields. The Higgs field now become

$$\phi = \frac{v + \eta + i\xi}{\sqrt{2}} = e^{i\xi \cdot \frac{\sigma}{2v}} \begin{pmatrix} 0 \\ \frac{v + \eta}{\sqrt{2}} \end{pmatrix}. \quad (2.28)$$

³⁷⁹ Due to $U(1)_{\text{EM}}$ invariance, a unitary gauge with the transformation $\phi \rightarrow \exp(-i\xi \cdot \frac{\sigma}{2v})$ can
³⁸⁰ be chosen to eliminate the massless bosons and incorporate them into the EM and weak
³⁸¹ bosons through the reparameterization in Equation 2.20. This leaves the massive η which
³⁸² can now be observed as an excitation of the Higgs field and consequently is the Higgs boson
³⁸³ h . Using the EW covariant derivative from Equation 2.17, the Higgs Lagrangian around the
³⁸⁴ vacuum state becomes

$$\begin{aligned} \mathcal{L}_H &= (D_\mu \phi)^\dagger (D^\mu \phi) - \mu^2 \left(\frac{v + h}{\sqrt{2}} \right)^2 - \lambda \left(\frac{v + h}{\sqrt{2}} \right)^4 \\ &= (D_\mu \phi)^\dagger (D^\mu \phi) - \frac{1}{2} \mu^2 h^2 - \lambda v h^3 - \frac{\lambda}{4} h^4 - \dots \end{aligned} \quad (2.29)$$

³⁸⁵ The Higgs mass can be extracted from the quadratic term as $m_H = \sqrt{-2\mu^2}$. The kinetic
³⁸⁶ term in the Lagrangian can be written as

$$\begin{aligned} (D_\mu \phi)^\dagger (D^\mu \phi) &= \frac{1}{2}(\partial_\mu h)^2 + \frac{g^2}{8}(v+h)^2 \left| W_\mu^1 - iW_\mu^2 \right|^2 + \frac{1}{8}(v+h)^2 (g'W_\mu - gB_\mu) \\ &= \frac{1}{2}(\partial_\mu h)^2 + (v+h)^2 \left(\frac{g^2}{4}W_\mu^+ W^{-\mu} + \frac{1}{8}(g^2 + g'^2) Z_\mu^0 Z^{0\mu} \right). \end{aligned} \quad (2.30)$$

³⁸⁷ Masses for the EW bosons can be extracted from the quadratic terms

$$m_{W^\pm} = \frac{v}{2}g, \quad m_Z = \frac{v}{2}\sqrt{g^2 + g'^2}, \quad m_\gamma = 0. \quad (2.31)$$

³⁸⁸ The fermion mass term $-m\bar{\psi}\psi$ still breaks EW invariance after spontaneous symmetry
³⁸⁹ breaking. Fermions instead acquire mass by replacing the mass term with a gauge invariant
³⁹⁰ Yukawa term in the EW Lagrangian for fermions' interactions with the Higgs field [8]

$$\begin{aligned} \mathcal{L}_{\text{Yukawa}} &= -c_f \frac{v+h}{\sqrt{2}} (\bar{\psi}_R \psi_L + \bar{\psi}_L \psi_R) \\ &= -\underbrace{\frac{c_f}{\sqrt{2}} v (\bar{\psi}\psi)}_{\text{fermion mass}} - \underbrace{\frac{c_f}{\sqrt{2}} (h\bar{\psi}\psi)}_{\text{fermion-Higgs interaction}}, \end{aligned} \quad (2.32)$$

³⁹¹ where c_f is the fermion-Higgs Yukawa coupling. The fermion mass is then $m_f = c_f v / \sqrt{2}$.

³⁹² 2.2 Beyond the Standard Model

³⁹³ 2.2.1 Top-philic vector resonance

³⁹⁴ Many BSM models extend the SM by adding to the SM gauge group additional $U(1)'$ gauge
³⁹⁵ symmetries, each with an associated vector gauge boson nominally named Z' [9]. In the case

396 of a BSM global symmetry group with rank larger than the SM gauge group, the symmetry
 397 group can break into $G_{\text{SM}} \times U(1)^{'n}$, where G_{SM} is the SM gauge group $SU(3)_C \times SU(2)_L \times$
 398 $U(1)_Y$ and $U(1)^{'n}$ is any $n \geq 1$ number of $U(1)'$ symmetries. The existence of additional
 399 vector bosons Z' would open up many avenues of new physics e.g. extended Higgs sectors
 400 from $U(1)'$ symmetry breaking, existence of flavor-changing neutral current (FCNC) effects
 401 in some models, and possible exotic production from heavy Z' decays [9].

402 Due to the top quark having the largest mass out of all known elementary particles in the SM,
 403 many BSM models [10–13] predict ‘top-philic’ vector resonances that have much stronger
 404 coupling to the top quark compared to other quarks such that the coupling factors to lighter
 405 quarks are negligible.

406 The analysis in this thesis attempts to reconstruct a top-philic Z' resonance directly to avoid
 407 dependency on model choice. In addition, a simplified color-singlet vector particle model
 408 [14, 15] is employed to study model-dependent interpretations. The interaction Lagrangian
 409 assumes only coupling with the top quark and has the form

$$\begin{aligned}
 \mathcal{L}_{Z'} &= \bar{t}\gamma_\mu (c_L P_L + c_R P_R) t Z'^\mu \\
 &= c_t \bar{t}\gamma_\mu (\cos \theta P_L + \sin \theta P_R) t Z'^\mu,
 \end{aligned} \tag{2.33}$$

410 where $c_t = \sqrt{c_L^2 + c_R^2}$ is the top coupling strength, $P_{L/R} = (1 \mp \gamma_5)/2$ are the chirality
 411 projection operators, and $\theta = \tan^{-1}(c_R/c_L)$ is the chirality mixing angle [14]. Expanding
 412 the Lagrangian results in

$$\mathcal{L}_{Z'} = \frac{1}{\sqrt{2}} \bar{t}\gamma_\mu \left[\sin \left(\theta + \frac{\pi}{4} \right) - \left(\sqrt{2} \cos \left(\theta + \frac{\pi}{4} \right) \right) \gamma_5 \right] t Z'^\mu, \tag{2.34}$$

⁴¹³ which bears striking resemblance to the neutral current interaction term in Equation 2.21,
⁴¹⁴ showing the similarity between the Z' and the neutral Z boson which acquires mass as a
⁴¹⁵ result of $U(1)_Y$ symmetry breaking.

⁴¹⁶ Assuming the Z' mass $m_{Z'}$ is much larger than the top mass ($m_t^2/m_{Z'}^2 \approx 0$), the Z' decay
⁴¹⁷ width at leading-order (LO) can be approximated as

$$\Gamma(Z' \rightarrow t\bar{t}) \approx \frac{c_t^2 m_{Z'}}{8\pi}. \quad (2.35)$$

⁴¹⁸ It can be observed that $\Gamma/m_{Z'} \approx c_t^2/8\pi \ll 1$ for $c_t \approx 1$. This suggests a very narrow and
⁴¹⁹ well-defined resonance peak, which supports efforts to directly reconstruct the resonance.

⁴²⁰ The main production channels for the aforementioned heavy topophilic color singlet Z' are
⁴²¹ at tree level and loop level, with the one-loop level being the dominant processes. Loop
⁴²² level processes are dependent on the chirality angle θ , where $\theta = \pi/4$ suppresses all but
⁴²³ gluon-initiated box subprocesses [14]. To minimize model dependence, only the tree level
⁴²⁴ production was considered and consequently $\theta = \pi/4$ was chosen for this analysis. The
⁴²⁵ Feynman diagrams for tree level production channels are shown in Figure 2.3.

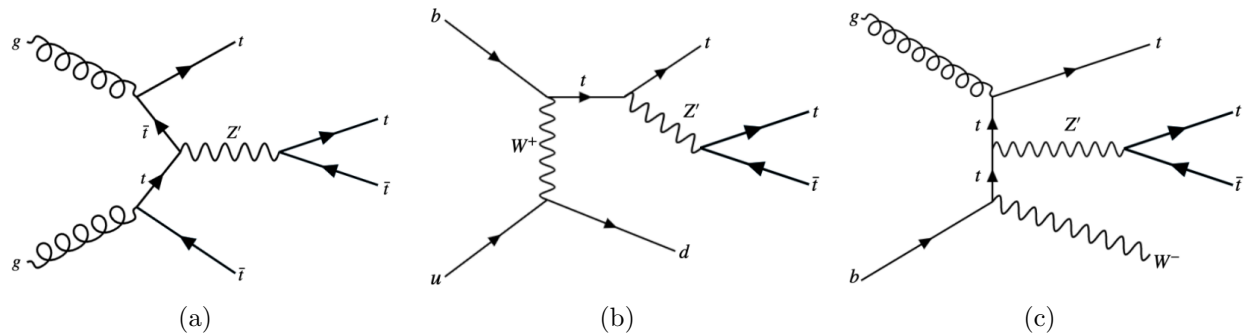


Figure 2.3: tree level Z' production in association with (a) $t\bar{t}$ to 4tops, (b) tj (light quark) to 3tops, (c) tW to 3 tops, derived from top quark final states produced via strong, EW and mixed QCD-EW interactions [14]

426 The single-top associated final states tjZ' and tWZ' productions are suppressed by three-
427 body phase space, resulting in smaller cross sections, by a factor of two, compared to the top
428 pair associated final state process $t\bar{t}Z' \rightarrow t\bar{t}t\bar{t}$. Unlike tjZ' and tWZ' which are produced by
429 EW and mixed QCD-EW interactions respectively, $t\bar{t}t\bar{t}$ production is governed by the strong
430 interaction only which can overpower phase space suppression.

431 Additionally, unlike $t\bar{t}t\bar{t}$ production which is independent of θ , single-top associated pro-
432 cesses are minimally suppressed under pure left-handed interaction ($\theta = 0$) and maximally
433 suppressed under pure right-handed interaction ($\theta = \pi/2$).

434 2.2.2 BSM four-top quark production

435 The analysis presented in this thesis uses the $t\bar{t}t\bar{t}$ final state signal signature to search for the
436 existence of a heavy BSM resonance that couples strongly to the top quark. Cross section
437 for $t\bar{t}t\bar{t}$ production can be enhanced by many possible BSM models, in particular possible
438 production of a heavy neutral resonance boson X , decaying to a $t\bar{t}$ pair, in association with
439 a $t\bar{t}$ pair in composite Higgs scenarios ([citations](#)) or two-Higgs-doublet-model (2HDM).

440 The $t\bar{t}X$ production mode and consequently $t\bar{t}t\bar{t}$ signal signature can provide a more sensitive
441 channel for searches by avoiding contamination from the large $gg \rightarrow t\bar{t}$ SM background in
442 an inclusive $X \rightarrow t\bar{t}$ search.

443 Decay modes

444 The different W boson decay modes shown in Figure 2.2 result in many different final states
445 for $t\bar{t}X/t\bar{t}t\bar{t}$ decay, which can each be classified into one of three channels: all hadronic decays;
446 exactly one lepton or two opposite-sign leptons (1LOS); exactly two same-sign leptons or

⁴⁴⁷ three or more leptons (SSML). The branching ratio for each channel is shown in Figure 2.4.
⁴⁴⁸ The all hadronic and 1LOS channels have much larger branching ratios compared to SSML
⁴⁴⁹ channel but suffer heavily from irreducible $gg \rightarrow t\bar{t}$ background contamination, giving SSML
⁴⁵⁰ channel better sensitivity at the cost of lower statistics. This is also the targeted channel for
⁴⁵¹ the analysis in this thesis.

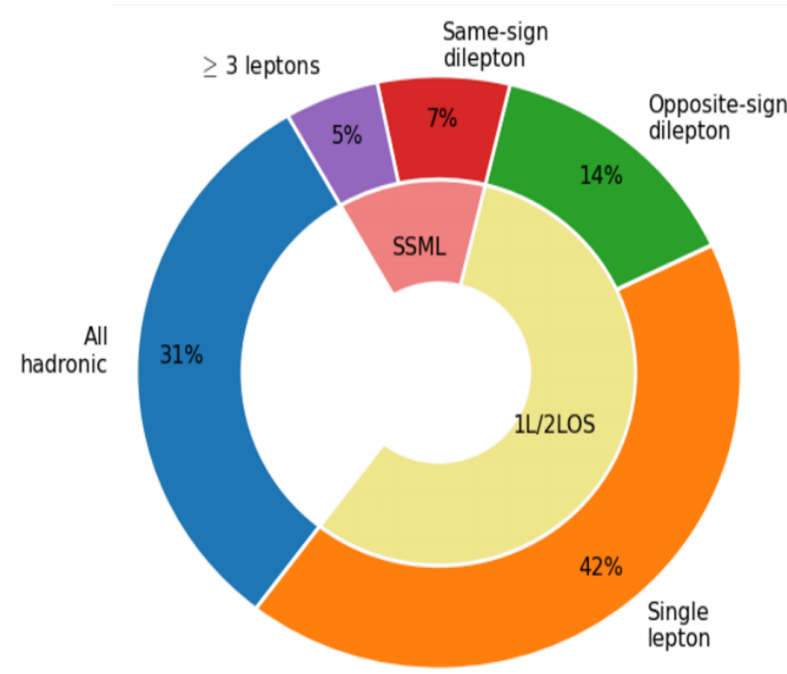


Figure 2.4: Caption

452 Chapter 3. LHC & ATLAS Experiment

453 3.1 The Large Hadron Collider

454 theoretical predictions are tested with experimental data obtained from particle accelerators
455 world's largest accelerator built by CERN situated on the border of Switzerland and France
456 has been operating since xxxx
457 lifetime divided into 3 runs, currently on Run 3 with planned upgrades on the horizon
458 responsible for a number of discoveries aka Higgs, etc.

459 3.1.1 Overview

460 [Basic info: location, size, main working mechanism, main detectors, main physics done]
461 - 27 km circumference, reusing LEP tunnels 175 m below ground level
462 - 7-13-13.6 TeV center of mass energies for pp collisions
463 - other than pp, also collides pPb, PbPb at 4 points with 4 main detectors: ATLAS, CMS
464 (general purpose detectors), ALICE (heavy ion physics, ion collisions), LHCb (*b*-physics)

465 3.1.2 LHC operations

466 - focuses mainly on pp collisions for this thesis - beams split into bunches of 1.1×10^{11}
467 protons with instantaneous luminosity of up to $2 \times 10^{34} \text{ cm}^{-2}\text{s}^{-1}$
468 - beam energies ramp up in other accelerators before injection, full ramp up to 6.5 GeV
469 about 20 minutes
470 (insert full diagram of accelerator chain)
471 Linac 4: hydrogen atoms, accelerated up to 160 MeV

⁴⁷² PSB: H atoms stripped of electrons before injection, accelerated to 2 GeV

⁴⁷³ PS: 26 GeV, SPS: 450 GeV

⁴⁷⁴ LHC: injection in opposite directions, 6.5 TeV per beam

⁴⁷⁵

⁴⁷⁶ Run 1: 2010-2012, Run 2: 2015-2018, Run 3: 2022-2025, HL-LHC: 2029-?

⁴⁷⁷ COM energies: 7 & 8 TeV, 13 TeV, 13.6 TeV, 13.6 & 14 TeV

⁴⁷⁸

⁴⁷⁹ inbetween periods: long shutdowns (LS1, LS2, LS3)

⁴⁸⁰



Figure 3.1: Caption [16]

Standard Model Production Cross Section Measurements

Status: October 2023

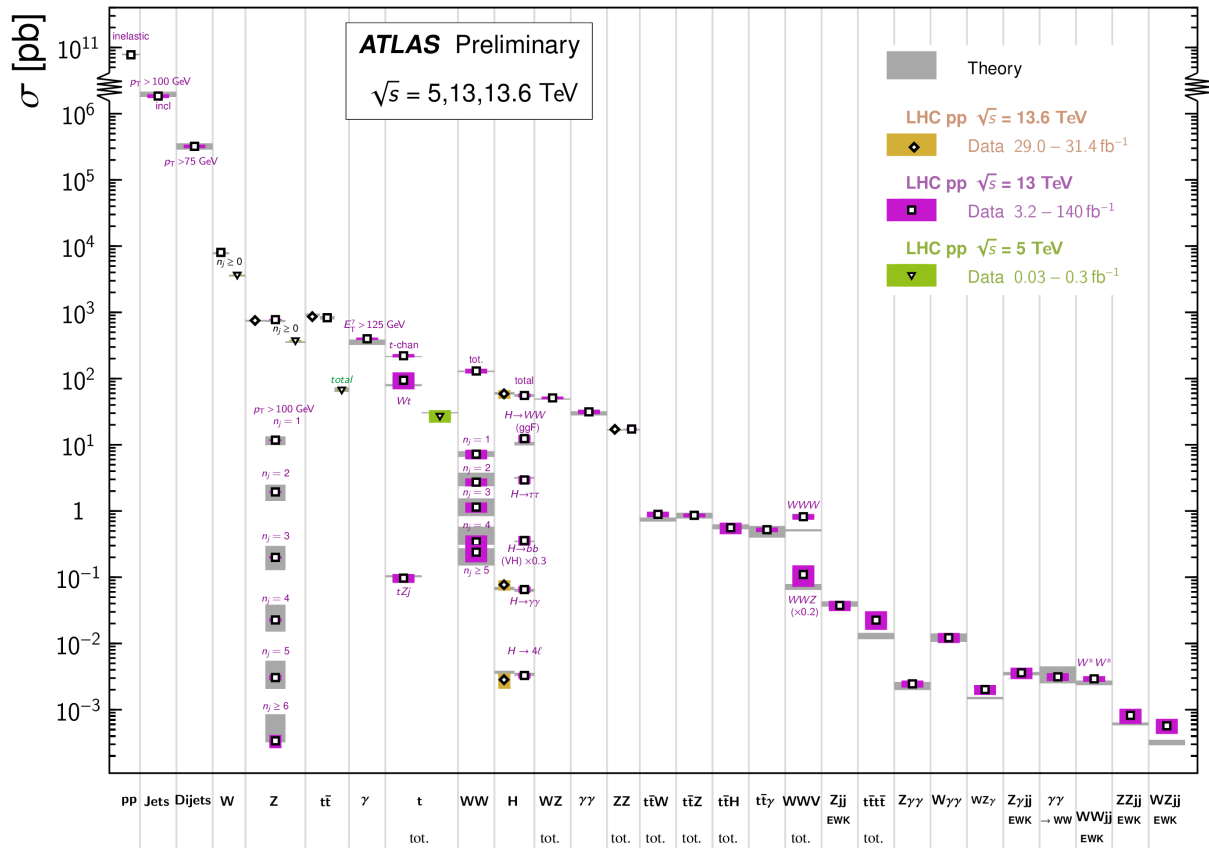


Figure 3.2: Caption [17]

481 Physics at the LHC

482 **3.2 The ATLAS detector**

483 multipurpose particle detector with a symmetric cylindrical geometry and a solid angle

484 coverage of almost 4π

485 44m long, 25m diameter

486 inner detector, solenoid/toroid magnet, EM & hadronic calorimeters, muon spectrometer

487 (insert figure)

488 right-handed cylindrical system, z-axis follows beamline, azimuthal and polar (0 in the

489 beam direction) angles measured with respect to beam axis.

490 pseudorapidity $\eta = -\ln \tan(\theta/2)$, approaches $\pm \infty$ along and 0 orthogonal to the beamline

491 distance $\Delta R = \sqrt{\Delta\eta^2 + \Delta\phi^2}$

492 transverse energy $E_T = \sqrt{p_T^2 + m^2}$

493 transverse momentum p_T component of momentum orthogonal to the beam axis $p_T =$

494 $\sqrt{p_x^2 + p_y^2}$

495 **3.2.1 Inner detector**

496 • measures tracks of charged particles with high momentum resolution ($\sigma_{p_T}/p_T = 0.05\% \pm 1\%$)

498 • covers particles with $p_T > 0.5$ GeV, $|\eta| < 2.5$

499 pixel detector -> semiconductor tracker -> transition radiation tracker, innermost to
500 outermost

501 • pixel detector:

- 502 – innermost, 250 μm silicon pixel layers
- 503 – detects charged particles from electron-hole pair production in silicon
- 504 – measures impact parameter resolution & vertex identification for reconstruction
- 505 of short-lived particles
- 506 – spatial resolution of 10 μm in the $R - \phi$ plane and 115 μm in the z-direction
- 507 – 80.4m readout channels
- 508 • sct:
- 509 – surrounds pixel detector, silicon microstrip layers with 80 μm strip pitch
- 510 – particle tracks cross 8 strip layers
- 511 – measures particle momentum, impact parameters, vertex position
- 512 – spatial resolution of 17 μm in the $R - \phi$ plane and 580 μm in the z-direction
- 513 – 6.3m readout channels.
- 514 • trt:
- 515 – outermost, layers of 4 mm diameter gaseous straw tubes with transition radiation
- 516 material ($70\% Xe + 27\% CO_2 + 3\% O_2$) & 30 μm gold-plated wire in the center
- 517 – tubes 144 cm length in barrel region ($|\eta| < 1$), 37 cm in the endcap region ($1 <$
- 518 $|\eta| < 2$), arranged in wheels instead of parallel to beamline)
- 519 – gas mixture produces transition radiation when ionized for electron identification
- 520 – resolution/accuracy of 130 μm for each straw tube in the $R - \phi$ plane
- 521 – 351k readout channels

522 3.2.2 Calorimeter systems

523 surrounds the inner detector & solenoid magnet, covers $|\eta| < 4.9$ and full ϕ range. Alternates
 524 passive and active material layers. Incoming particles passing through calorimeter produce
 525 EM cascades or hadronic showers in passive layer. Energies deposited and convert to electric
 526 signals in active layers for readout.

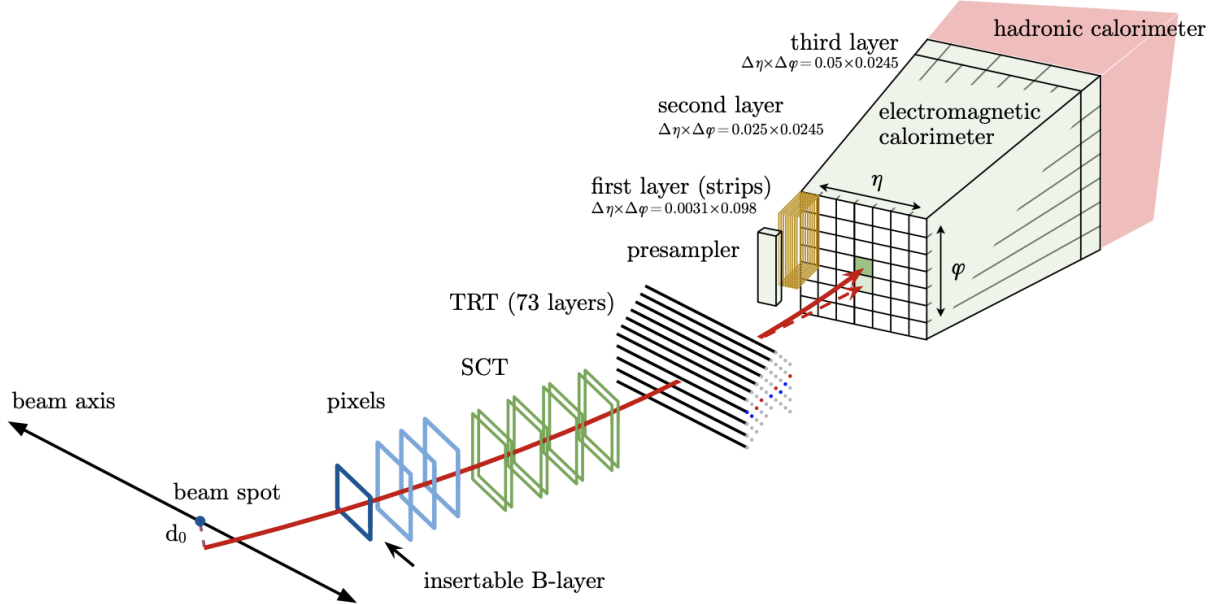


Figure 3.3: Caption [31]

527 EM calorimeter:

- 528 • innermost, lead-LAr detector (passive-
529 active)
- 530 • measures EM cascades (bremsstrahlung
531 & pair production) produced by elec-
532 trons/photons

533 • divided into barrel region ($|\eta| < 1.475$)

534 & endcap regions ($1.375 < |\eta| < 3.2$)
535 with transition region ($1.372 < |\eta| <$
536 1.52) containing extra cooling materi-
537 als for inner detector

538 • end-cap divided into outer wheel

539 (1.372 < $|\eta|$ < 2.5) & inner wheel

540 (2.5 < $|\eta|$ < 3.2) 556

- 541 • higher granularity in ID ($|\eta| < 2.5$)
542 range for electrons/photons & precision 558
543 physics, coarser elsewhere for jet recon-
544 struction & MET measurements 559

545 hadronic calorimeter: 560

- 546 • outermost 561
- 547 • measures hadronic showers from inelas- 562
548 tic QCD collisions 563
- 549 • thick enough to prevent most particles 564
550 showers from reaching muon spectrom- 565
551 eter 566
- 552 • split into tile calorimeter in barrel re- 567
553 gion ($|\eta| < 1.0$) & extended barrel re- 568
554 gion ($0.8 < |\eta| < 1.7$), LAr hadronic 569

end-cap calorimeter (HEC) in end-cap regions ($1.5 < |\eta| < 3.2$) & LAr forward calorimeters (FCal) in $3.1 < |\eta| < 4.9$ range.

- tile calorimeters: steel-plastic scintillating tiles, readout via photomultiplier tubes
- hec: behind tile calorimeters, 2 wheels per end-cap. copper plates-LAr. overlap with other calorimeter systems to cover for gaps between subsystems
- fcal: 1 copper module & 2 tungsten modules-LAr. copper optimized for EM measurements, tungsten for hadronic.

571 3.2.3 Muon spectrometer

- 572 • ATLAS outermost layer. measures muon momenta & charge in range $|\eta| < 2.7$

573 • momentum measured by deflection in track from toroid magnets producing magnetic

574 field orthogonal to muon trajectory

575 – large barrel toroids in $|\eta| < 1.4$, strength 0.5 T

- 576 – 2 smaller end-cap toroids in $1.6 < |\eta| < 2.7$, strength 1 T
- 577 – transition region $1.4 < |\eta| < 1.6$, deflection provided by a combination of barrel
- 578 and end-cap magnets
- 579 • chambers installed in 3 cylindrical layers, around the beam axis in barrel region & in
 - 580 planes perpendicular to beam axis in the transition and end-cap regions
 - 581 • split into high-precision tracking chambers (monitored drift tubes & cathode strip
 - 582 chambers) & trigger chambers (resistive plate chambers & thin gap chambers)
 - 583 • trigger chambers provide fast muon multiplicity & approximate energy range informa-
 - 584 tion with L1 trigger logic

- 585 – mdt:
- 586 * range $|\eta| < 2.7$, innermost layer⁵⁹⁹
- 587 $|\eta| < 2.0$
- 588 * precision momentum measure⁶⁰¹
- 589 ment
- 590 * layers of 30 mm drift tubes filled⁶⁰¹
- 591 with 93% Ar & 7% CO₂, with⁶⁰¹
- 592 a 50 μm gold-plated tungsten⁶⁰⁵
- 593 rhodium wire at the center
- 594 * muons pass through tube, ioniz⁶⁰⁷
- 595 izing gas and providing signals⁶⁰⁸
- 596 Combining signals from tubes⁶⁰⁹
- 597 forms track
- 598 * maximum drift time from wall
- 600 to wire 700 ns
- 602 * resolution: 35 μm per chamber,
- 604 80 μm per tube
- 606 – csc:
- 608 * forward region $2.0 < |\eta| < 2.7$,
- 610 highest particle flux and density
- 612 region
- 614 * multiwire proportional chambers
- 616 with higher granularity, filled
- 618 with 80% Ar & 20% CO₂
- 620 * shorter drift time than MDT,
- 622 plus other features making CSC

611 suitable for high particle densities – rpc:
612 and consequently able to * range $|\eta| < 1.05$
613 handle background conditions * provide fast meas
614 * resolution: 40 μm in bending η -
615 plane, 5 mm in nonbending ϕ -
616 plane due to coarser cathode seg-
617 mentation, per CSC plane

623 3.2.4 Forward detectors

- 624 • LUCID (LUminosity measurement using Cherenkov Integrating Detector): ± 17 m from
625 interaction point, measures luminosity using pp scattering in the forward region
- 626 • ALFA (Absolute Luminosity for ATLAS): ± 240 m, measures pp scattering at small
627 angles
- 628 • ZDC (Zero-Degree Calorimeter): ± 140 m, measures centrality in heavy-ion collisions

629 3.2.5 Magnetic systems

630 superconducting solenoid & toroid magnets cooled to 4.5 K with liquid helium
631 solenoid: 2.56 m diameter, 5.8 m length, 2 T strength axial magnetic field, encloses inner
632 detector
633 toroid = barrel + endcap toroid x2
634 barrel toroid: 9.2/20.1 m inner/outer diameter, 25.3 m length, 0.5 T strength
635 endcap toroid: 1.65/10.7 m inner/outer diameter, 5 m length, 1 T strength
636 (show magnet system diagram)

637 3.2.6 Trigger & data acquisition

638 LHC produces large amount of data (40 MHz with 25 ns bunch crossing), necessitates a way
639 to filter out trash from interesting events
640 handles online processing, selecting and recording interesting events for further offline pro-
641 cessing and more in-depth analyses

642

- 643 • Level-1 (L1) trigger: online, fast hardware-based trigger, reduces to 100 kHz
 - 644 – L1 calorimeter triggers (L1Calo): selects high energy objects & MET
 - 645 – L1 muon triggers (L1Muon): selects using hit information from RPC & TGC
 - 646 – L1 topological trigger (L1Topo): select based on topological selection synthesized
 - 647 using information from L1Calo & L1Muon
 - 648 – Central Trigger Processor (CTP): uses L1Calo/Muon/Topo for final L1 trigger
 - 649 decision within 2.5 μ s latency. Also identify regions of interest in η and ϕ to be
 - 650 processed directly by HLT
- 651 • L1 trigger information read out by Front-End (FE) detector electronics then sent to
 - 652 ReadOut Drivers (ROD) for preprocessing and subsequently to ReadOut System (ROS)
 - 653 to buffer
- 654 • High-Level Trigger (HLT): offline, software-based trigger, using dedicated algorithms
 - 655 and L1 output as input, reduces to 1 kHz
- 656 • Send to storage for analyses after HLT

657 overall trigger process reduces original collision data rate by a factor of about 10000 after

658 HLT

659 (show TDAQ diagram)

660 Chapter 4. Particle Reconstruction & Identification

662 Reconstruction software reconstructs basic objects from signals collected from the event:
663 interaction vertices, tracks, topological clusters of energy deposits
664 These quantities then used to reconstruct physics objects i.e. particles (electron, muon),
665 jets, MET

666 4.1 Primary reconstruction

667 4.1.1 Topological clusters

668 [18][19]

669 Topological cluster (topo-cluster): Clusters of topologically connected cell signals in the
670 calorimeter at the EM scale. This scale does not consider loss of signal from hadrons. Sin-
671 gular hits without hits from neighboring cells are considered noise.

672 Done in an effort to extract signal while minimizing electronic effects and physical fluctua-
673 tions. Used to reconstruct hadronic objects and particles decaying hadronically i.e. τ leptons

674 Signal hits with significance above a cell signal significance level $\zeta_{\text{cell}}^{\text{EM}}$ are seeded in as part
675 of a proto-cluster. Neighboring cells satisfying a cluster growth threshold are collected into
676 the cluster.

677 Two clusters are merged if a cell is matched to both

678 If a cluster has two or more local signal maxima satisfying $E_{\text{cell}}^{\text{EM}} > 500 \text{ MeV}$, the cluster is
679 split accordingly.

680 The process continues iteratively until all cells with significant signal efficiency have been
681 matched to a cluster.

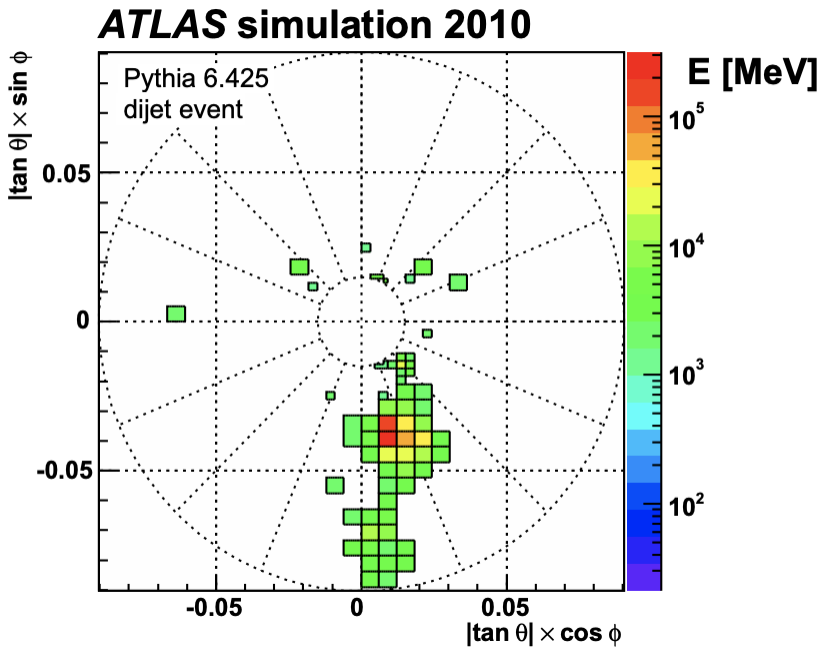


Figure 4.1

682

683 4.1.2 Tracks

684 [20]

685 Charged particles deposit energy in different layers of the inner detector and muon spec-
686 trometer

687 ID reco software: inside-out and outside-in algorithms

688

689 • Inside-out: [21]

690 Starts with seeded hits in the silicon detector in pixel & SCT

691 Loosely matched to an EM cluster to form a track candidate
692 Hits are added to form a track candidate using a pattern recognition algorithm based
693 on a Kalman filter formalism [22]
694 Track candidates are then fitted with a χ^2 filter [23] and loosely matched to a fixed-sized
695 EM cluster. Successfully matched track candidates are re-fitted with a Gaussian-sum
696 filter (GSF) [24]
697 This is followed by a track scoring strategy to resolve fake tracks & hit ambiguity
698 between different tracks [25]
699 Extend to TRT to form final tracks, filtered by threshold $p_T > 400$ MeV.

700

701 • Outside-in: [26]
702 Reverse, starts with segments in TRT extending inward to silicon hits in pixel & SCT
703 Targeting secondary tracks (decays/interactions of primary particles) or long-lived par-
704 ticles

705 4.1.3 Vertices

706 Vertices: interaction or decay point
707 Primary vertex: pp interaction point
708 Important for reconstruction of the hard scattering pp interaction, resulting trajectories and
709 kinematic information of the event

710

711 • Vertex finding:
712 Uses the z-position of a track as input

713 Vertices require to have at least 2 tracks

714 Iterative χ^2 algorithm evaluate track-vertex compatibility, using the track as new seed

715 for another vertex if large discrepancy

716 • Vertex fitting:

717 Adaptive multi-vertex fitter (AVF) algorithm assigns weights that depend on the track-

718 vertex compatibility to each track to measure the probability of the track being an

719 outlier vs inlier.

720 Vertex is then estimated by iteratively minimizing an objective function of these

721 weights

722 4.2 Jets

723 - Quarks, gluons & other non-color-neutral hadrons cannot be observed individually due to

724 QCD color confinement

725 - A non-color-neutral hadron will almost immediately undergo hadronization producing a

726 cone of color-neutral hadrons also known as a jet

727 - Jet signals can be used to reconstruct and consequently indirectly observe the original

728 quarks/gluons the jets originated from

729 - Jet reconstruction:

- 730 • PFlow: energy deposited in the calorimeter systems by charged particles is removed
- 731 and replaced by particle objects created with the remaining energy in the calorimeter
- 732 and tracks matched to the topo-clusters. (include PFlow graphics)
- 733 • anti- k_t algorithms: sequential recombination jet algorithms

- 734 • pile-up jets: multiple interactions associated with one bunch crossing in addition to the
 735 hard scattering of interest and reconstructed as jets in the final states. Reconstructed
 736 pile-up jets can result from Pile-up jets are usually from soft interactions and can be
 737 distinguished with JVT algorithm using tracking information from the ID.

 738 • JES/JER calibration: Jet reconstruction at EM scale does not accurately account
 739 for energy from QCD interactions and needs to be calibrated to jets reconstructed at
 740 particle level. This is done via a MC-based JES calibration sequence and additional
 741 JER calibration to match jet resolution in simulation to data using dijet events.

 742 For this analysis, jets are reconstructed using PFlow method with anti- k_t algorithm,
 743 using radius parameter $\Delta R = 0.4$.

 744 JVT applied to reconstructed jets with $p_T < 60$ GeV and $|\eta| < 2.4$.

745 **4.2.1 Flavor tagging**

- 746 - Classification of hadronic jets is an important task for many LHC analyses especially ones
 747 studying final states (Higgs decay/4top)

 748 - Flavor tagging is namely interested in identifying jets containing b -hadrons, c -hadrons,
 749 uds -hadrons (light-jets), and hadronic decays from τ .

 750 - Of these, identifying b -jets is of particular interest due to their characteristically long
 751 lifetime (≈ 1.5 ps) from decay suppression by CKM factor, with a displaced secondary decay
 752 vertex and usually a tertiary vertex from c -hadron decays.

753 **Efficiency calibration**

754 - [27]

755 - Performance of b -taggers are studied on MC simulated samples. However, the b -tagging
756 efficiency predicted by simulation $\varepsilon_b^{\text{sim}}$ is usually not the same as the efficiency measured in
757 data $\varepsilon_b^{\text{data}}$.

758 - The correction for the rate of events after applying a b -tagging requirement is calibrated
759 and applied jet by jet in the form of data-to-simulation scale factors $\text{SF} = \varepsilon_b^{\text{data}} / \varepsilon_b^{\text{sim}}$.

760 - Usage of b -tagger in this analysis is done via five operating points (OPs), corresponding
761 to 60%, 70%, 77%, 85% and 90% b -jet tagging efficiency ε_b in simulated $t\bar{t}$ events in order
762 from loosest to tightest discriminant cut points. - OPs are defined by selection on the tagger
763 output to provide a pre-defined level of ε_b , and act as a variable trade-off between b -tagging
764 efficiency and c -/light-jet rejection i.e. b -jet purity

765 - A jet is considered b -tagged if it passes the efficiency criteria for a given OP. A pseudo-
766 continuous b -tagging (PCBT) score is defined to summarize the OP criteria a jet passes into
767 a variable. The PCBT score can take integer values between 1 and 6, where a score of 6
768 means a jet passes all four OP thresholds (passing 65% OP), a score of 2 for jets that pass
769 only the 90% OP, and a score of 1 for jets that don't pass any OP. Additionally, PCBT
770 defines a value of -1 for any jet that does not satisfy b -tagging criteria.

771

772 - For this analysis,jets containing b -hadrons are identified and tagged with the GN2v01
773 algorithm, described in subsection 4.2.1. A jet is considered b -tagged if it passes the 85%
774 WP; this gives the best sensitivity to the signal out of all five possible b -tagging WPs. The
775 b -tagged jet is then assigned a PCBT score accordingly.

776 btag optimization table?

777 GN2 *b*-tagging algorithm

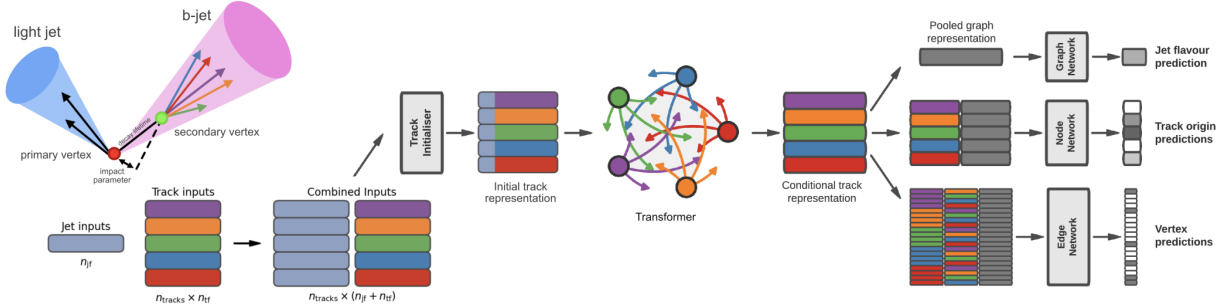


Figure 4.2: Caption [28–30]

778 - GN2 transformer-based *b*-tagging algorithm, utilized for analysis of Run 2 and Run 3

779 data

780 - GN2 gives a factor of 1.5-4 improvement in experimental applications compared to the
781 previous convolutional neural network-based standard *b*-tagging algorithm, DL1d, without
782 dependence on the choice of MC event generator.

783 - Attention-based architecture, modified to incorporate domain knowledge and additional
784 auxiliary physics objectives: grouping tracks originating from common vertices and predic-
785 tion of the underlying process for each track

786 - MC simulated SM $t\bar{t}$ and BSM Z' events from pp collisions were used as training and
787 evaluation samples. In order to minimize bias, both *b*- and light-jet samples are re-sampled
788 to match *c*-jet distributions.

789 - GN2 concatenates 2 jet and 19 track reconstruction variables of up to 40 tracks to form
790 the input feature vector, normalized to zero mean and unit variance.

791 - The output consists of a jet classification layer of size 4 consisting of p_b , p_c , p_u and p_τ for

792 the probability of each jet being a b -, c -, light- or τ -jet respectively; a track-pairing output
793 layer of size 2, and a track origin classification layer of 7 output categories.

794 4.3 Leptons

795 - Lepton reconstruction is concerned mainly with electron and muon construction, since tau
796 decays quickly and can either be reconstructed using jets or light leptons. From here on out
797 lepton will be used mostly to refer to electrons and muons
798 - Leptons can be classified into two categories: prompt leptons resulting from heavy particle
799 decays, or non-prompt leptons resulting from detector or reconstruction effects, or from b -
800 or c - hadron decays
801 - Reconstruction of leptons is therefore important to study the underlying physics and sup-
802 pressing background

803 4.3.1 Electrons

804 - [31][32]
805 - Electrons lose energy interacting with the detector materials via bremsstrahlung. The
806 bremsstrahlung photon can then produce an electron-positron pair which can itself leaves
807 signals in the detector, creating a collimated object that can leave multiple tracks in the ID
808 or EM showers in the calorimeter, all considered part of the same EM topo-cluster.
809 - Electron signal signature has three characteristic components: localized energy deposits
810 in the calorimeter, multiple tracks in the ID and compatibility between the above tracks
811 and energy clusters in the $\eta \times \phi$ plane. Electron reconstruction in ATLAS follows these
812 steps accordingly - Electron path through the detector is shown in Figure 3.3 - Seed-cluster

813 reconstruction and track reconstruction are performed sequentially in accordance with the
814 iterative clustering algorithm and track reconstruction method respectively, described in
815 section 4.1

816 - The seed-cluster and track candidate associated with a conversion vertex are then matched
817 to form an electron candidate.

818 - A reconstructed cluster is expanded from the seed-cluster in either ϕ or η in the barrel or
819 endcap region respectively

820 - The cluster energy is then calibrated to compute the original electron energy.

821 Electron identification

822 - Additional likelihood-based identification selections using ID and EM calorimeter infor-
823 mation are implemented to further improve the purity of the reconstructed electrons and
824 photons. These selections also help suppress background from hadronic jet deposits, photon
825 conversions or electrons from heavy-flavor decays.

826 - Three operating points are defined for physics analyses: Loose, Medium and Tight, op-
827 timized for 9 bins in $|\eta|$ and 12 bins in E_T with each corresponding to a fixed efficiency
828 requirement for each bin. The target efficiencies for Loose, Medium and Tight start at 93%,
829 88% and 80% respectively for typical EW processes and increases with E_T

830 Similar to b -tagging OPs, the electron OPs represent a trade-off in signal efficiency and back-
831 ground rejection. The electron efficiency are estimated using tag-and-probe method [31] on
832 samples of $J/\Psi \rightarrow ee$ and $Z \rightarrow ee$ [32].

⁸³³ **Electron isolation**

- A characteristic distinction between prompt electrons and electrons from background processes is the relative lack of activity in both the ID and calorimeter within an area of $\Delta\eta \times \Delta\phi$ surrounding the reconstruction candidate
- Electron isolation variables are needed to quantify the amount of activity around the electron candidate.
- Calorimeter-based isolation variables $E_T^{\text{cone}XX}$ is calculated by first summing the energy of topological clusters with barycenters falling within a cone of radius $\Delta R = \sqrt{(\Delta\eta)^2 + (\Delta\phi)^2} = XX/100$ around the direction of the electron candidate.
- The final isolation variable is then obtained by subtracting energy at the core of the cone belonging to the candidate electron from the sum, then applying corrections for energy leakage outside of the core and pile-up effects.
- Similar to calorimeter-based variables, track-based isolation variables $p_T^{\text{varcone}XX}$ are calculated by summing all track p_T within a cone of variable radius ΔR around the electron candidate, minus the candidate's contribution. The cone radius is variable as a function of p_T

$$\Delta R = \min \left(\frac{10}{p_T[\text{GeV}]}, \Delta R_{\max} \right)$$

- ⁸³⁴ with ΔR_{\max} being the maximum cone size, to account for the closer proximity of decay products to the electron in high-momentum heavy particle decays.
- ⁸³⁵ - Four isolation operating points are implemented to satisfy specific needs by physics analyses:
- ⁸³⁶ Loose, Tight, HighPtCaloOnly and Gradient. The first three OPs are fixed in isolation
- ⁸³⁷ variables, while the Gradient OP fixes the isolation efficiency to a p_T dependent function
- ⁸³⁸ defined as $\varepsilon = 0.1143 \times p_T + 92.14\%$ with p_T in GeV, using $\Delta R = 0.2$ for calorimeter isolation

840 and $\Delta R_{\text{max}} = 0.2$ for track isolation[32].

841 Electron charge misidentification

842 [31][33]

843 Electron charge is determined by the curvature of the associated track. Misidentification
844 of charge can then occur via either an incorrect curvature measurement, or an incorrectly
845 matched track.

846 The former is more likely for electrons with high p_T due to the small curvature in track tra-
847 jectories at such scale, while the latter usually results from bremsstrahlung pair-production,
848 creating additional secondary tracks in the vicinity.

849 Charge misidentification is a crucial irreducible background for analyses with charge selection
850 criteria, and suppression of this background is assisted via a boosted decision tree discrim-
851 inant known as the Electron Charge ID Selector (ECIDS) [31]. The addition of ECIDS
852 removed 90% of electrons with incorrect charge while selecting 98% of electrons with correct
853 charge from electrons in $Z \rightarrow ee$ events satisfying Medium/Tight identification and Tight
854 isolation criteria.

855 4.3.2 Muons

856 Signature: minimum-ionizing particle leaves tracks in the MS or characteristics energy de-
857 posits in the calorimeter

858 Muons can be reconstructed globally using information from the ID, MS and calorimeters.
859 Five reconstruction strategies, each corresponding to a muon type:

- 860 • Combined (CB): primary ATLAS muon reconstruction method. Muons first recon-
861 structed using MS tracks then extrapolated to include ID tracks (outside-in strategy).

862 A global combined fit is then performed on both MS and ID tracks

- 863 • Inside-out combined (IO): Complementary to CB algorithm. Muon tracks are extrap-
864 olated from ID to MS, then fitted together with a combined track fit. Useful for muons
865 without good MS information.
- 866 • MS extrapolated (ME): ME muons are defined as muons with a MS track that cannot
867 be matched to an ID track using CB method. ME muons allow extension of muon
868 reconstruction acceptance to regions not covered by the ID ($2.5 < |\eta| < 2.7$)
- 869 • Segment-tagged (ST): ST muons are ID tracks satisfying tight angular matching cri-
870 teria to at least one reconstructed local segment in the MDT or CSC chambers when
871 extrapolated to the MS. Used primarily when muons only crossed one layer of MS
872 chambers.
- 873 • Calorimeter-tagged (CT): CT muons are ID tracks that when extrapolated through the
874 calorimeter, can be matched to energy deposits consistent with those of a minimum-
875 ionizing particle. Extends acceptance range to regions in the MS with sparse instrumen-
876 tation ($|\eta| < 0.1$), with a higher p_T threshold of 5 GeV compared to 2 GeV threshold
877 used by other muon reconstruction algorithms due to large background contamination
878 at the low p_T range of $15 < p_T < 100$ GeV

879 Muon identification

880 [34][35]

881 Reconstructed muons are further filtered by identification criteria to select for high-quality
882 prompt muons for physics analyses. Requirements include number of hits in the MS/ID,
883 track fit properties and compatibility between measurements of the two systems.

884 Three standard WPs (Loose, Medium, Tight) are defined to better match the needs of differ-
885 ent physics analyses concerning prompt muon ID efficiency, p_T resolution and non-prompt
886 muon rejection. Of the three, Medium WP is the default ID WP for ATLAS, by virtue
887 of being optimized in efficiency and purity for a wide range of analyses while minimizing
888 non-prompt rejection and systematic uncertainties[34].

889

890 Muon isolation

891 Muons from heavy particle decays are often produced in an isolated manner compared to
892 muons from semileptonic decays. Muon isolation is therefore an important tool for back-
893 ground rejection in physics analyses

894 Muon isolation strategies are similar to that of electron in subsection 4.3.1, with track-based
895 and calorimeter-based isolation variables.

896 Seven isolation WPs are defined to satisfy analyses' needs.

897 4.4 Missing transverse momentum

898 [36]

899 Collisions at the LHC happen along the z-axis of the ATLAS coordination system between
900 two particle beam of equal center-of-mass energy. By conservation of momentum, the sum
901 of transverse momenta of outgoing particles should be zero. A discrepancy between mea-
902 sured momentum and zero would then suggest the presence of undetectable particles, which
903 would consist of either SM neutrinos or some unknown BSM particles. This makes missing
904 transverse momentum (E_T^{miss}) an important observable to reconstruct.

905 Reconstructing E_T^{miss} utilizes information from fully reconstructed leptons, photons, jets
 906 and other matched track-vertex objects not associated with a prompt object (soft signals),
 907 defined with respect to the $x(y)$ -axis as

$$E_{x(y)}^{\text{miss}} = - \sum_{i \in \{\text{hard objects}\}} p_{x(y),i} - \sum_{j \in \{\text{soft signals}\}} p_{x(y),j}, \quad (4.1)$$

where $p_{x(y)}$ is the $x(y)$ -component of p_T for each particle. The following observables can then be defined:

$$\mathbf{E}_T^{\text{miss}} = (E_x^{\text{miss}}, E_y^{\text{miss}}), \quad (4.2)$$

$$E_T^{\text{miss}} = |\mathbf{E}_T^{\text{miss}}| = \sqrt{(E_x^{\text{miss}})^2 + (E_y^{\text{miss}})^2}, \quad (4.3)$$

$$\phi^{\text{miss}} = \tan^{-1}(E_y^{\text{miss}}/E_x^{\text{miss}}), \quad (4.4)$$

908 where E_T^{miss} represents the magnitude of the missing transverse energy vector $\mathbf{E}_T^{\text{miss}}$, and
 909 ϕ^{miss} its direction in the transverse plane. Since physics analyses have differing requirements
 910 for object selection, the vectorial sum $\mathbf{E}_T^{\text{miss}}$ can be broken down into

$$\mathbf{E}_T^{\text{miss}} = - \underbrace{\sum_{\substack{\text{selected} \\ \text{electrons}}} \mathbf{p}_T^e - \sum_{\substack{\text{selected} \\ \text{muons}}} \mathbf{p}_T^\mu - \sum_{\substack{\text{accepted} \\ \text{photons}}} \mathbf{p}_T^\gamma - \sum_{\substack{\text{accepted} \\ \tau\text{-leptons}}} \mathbf{p}_T^\tau}_{\text{hard term}} - \underbrace{\sum_{\substack{\text{accepted} \\ \text{jets}}} \mathbf{p}_T^{\text{jet}} - \sum_{\substack{\text{unused} \\ \text{tracks}}} \mathbf{p}_T^{\text{track}}}_{\text{soft term}}. \quad (4.5)$$

911 Two WPs are defined for E_T^{miss} , Loose and Tight [37], with selections on jet p_T and JVT
 912 criteria. The Tight WP is used in this analysis, and reduces pileup dependence of E_T^{miss} by
 913 removing the phase space region with more pileup jets than hard-scatter jets, at the expense
 914 of resolution at low pileup and scale of the reconstructed E_T^{miss} .

₉₁₅ **4.5 Overlap removal**

₉₁₆ Since the reconstruction processes for different objects are performed independently, it is
₉₁₇ possible for the same detector signals to be used to reconstruct multiple objects. An overlap
₉₁₈ removal strategy to resolve ambiguities; the overlap removal process for this analysis applies
₉₁₉ selections listed in Table 4.1 sequentially, from top to bottom.

Table 4.1: Caption [38]

Remove	Keep	Matching criteria
Electron	Electron	Shared ID track, $p_{T,1}^e < p_{T,2}^e$
Muon	Electron	Shared ID track, CT muon
Electron	Muon	Shared ID track
Jet	Electron	$\Delta R < 0.2$
Electron	Jet	$\Delta R < 0.4$
Jet	Muon	($\Delta R < 0.2$ or ghost-associated) & $N_{\text{track}} < 3$
Muon	Jet	$\Delta R < \min(0.4, 0.04 + 10\text{GeV}/p_T^\mu)$

₉₂₀ **4.6 Object definition**

₉₂₁ Table 4.2 shows the selections used in this analysis. Each selection comes with associated
₉₂₂ calibration scale factors to account for discrepancies between data and MC simulation, and
₉₂₃ are applied multiplicatively to the MC event weights.

Table 4.2: Caption

Selection	Electrons	Muons	Jets
p_T [GeV]	> 15 $p_T(l_0) > 28$	> 15	> 20
$ \eta $	$1.52 \leq \eta < 2.47$ < 1.37	< 2.5	< 2.5
Identification	TightLH pass ECIDS ($ee/e\mu$)	Medium	NNJvt FixedEffPt ($p_T < 60$, $ \eta < 2.4$)
Isolation	Tight_VarRad	PflowTight_VarRad	
Track-vertex assoc.			
$ d_0^{\text{BL}}(\sigma) $	< 5	< 3	
$ \Delta z_0^{\text{BL}} \sin \theta $ [mm]	< 0.5	< 0.5	

924 **Chapter 5. Data & Simulated Samples**

925 **5.1 Data samples**

926 LHC Run 2 data collected at $\sqrt{s} = 13$ TeV between 2015-2018

927 luminosity 140 fb^{-1}

928 (include uncertainty for Run 2 only)

Triggers used:

Table 5.1: Caption

Trigger	Data period			
	2015	2016	2017	2018
Single electron triggers				
HLT_e24_lhmedium_L1EM20VH	✓	-	-	-
HLT_e60_lhmedium	✓	-	-	-
HLT_e120_lhloose	✓	-	-	-
HLT_e26_lhtight_nod0_ivarloose	-	✓	✓	✓
HLT_e60_lhmedium_nod0	-	✓	✓	✓
HLT_e140_lhloose_nod0	-	✓	✓	✓
Di-electron triggers				
HLT_2e12_lhloose_L12EM10VH	✓	-	-	-
HLT_2e17_lhvloose_nod0	-	✓	-	-
HLT_2e24_lhvloose_nod0	-	-	✓	✓
HLT_2e17_lhvloose_nod0_L12EM15VHI	-	-	-	✓
Single muon trigger				
HLT_mu20_iloose_L1MU15	✓	-	-	-
HLT_mu40	✓	-	-	-
HLT_mu26_ivarmedium	-	✓	✓	✓
HLT_mu50	-	✓	✓	✓

929

930 **5.2 Monte Carlo samples**

931 Monte Carlo simulated samples are used to estimate signal acceptance before unblinding,
932 profile the physics background for the analysis and to study object optimizations.
933 Simulated samples for this analysis use are generated from ATLAS' generalized MC20a/d/e
934 samples for Run 2, using full detector simulation (FS) based on Geant4.

935 **5.2.1 $t\bar{t}Z'$ signal samples**

936 Run 2 $t\bar{t}Z'$ sample
937 samples: 6 samples for each mass point from [1, 1.25, 1.5, 2, 2.5, 3] TeV
938 generator: MADGRAPH5_AMC@NLO v.2.8.1p3.atlas9 at LO with NNPDF3.1LO pdf
939 event: PYTHIA8 [v.244p3.rangefix] using A14 tune & NNPDF2.3LO pdf

940 parameters:

- 941 • chirality angle $\theta = \pi/4$ as discussed in subsection 2.2.1
942 • top- Z' coupling $c_t = 1$

943 resonance width computed with MADGRAPH5_AMC@NLO to be 4% of model configuration
944 with these parameters

945 **5.2.2 Background samples**

946 Run 2 mc20 samples (2015-2018)
947 (explain most important backgrounds: $t\bar{t}t\bar{t}$ & $t\bar{t}V$, $t\bar{t}$

Table 5.2: Summary of all Monte-Carlo samples used in this analysis.

Process	ME Generator	ME Order	ME PDF	PS	Tune	Sim.
Signals						
$t\bar{t}Z'$	MADGRAPH5_AMC@NLO LO		NNPDF3.1LO	PYTHIA8 A14		FS
$t\bar{t}\bar{t}$ and $t\bar{t}t$						
$t\bar{t}\bar{t}$	MADGRAPH5_AMC@NLO NLO MADGRAPH5_AMC@NLO NLO	NLO	NNPDF3.0nlo MMHT2014LO	PYTHIA8 A14 HERWIG7 H7-UE-MMHT	AF3 AF3	
$t\bar{t}t$	SHERPA	NLO	NNPDF3.0 NNLO	HERWIG7 SHERPA	FS	
$t\bar{t}t$	MADGRAPH5_AMC@NLO LO		NNPDF2.3lo	PYTHIA8 A14	AF3	
$t\bar{t}V$						
$t\bar{t}H$	POWHEGBOX v2	NLO	NNPDF3.0nlo (mc20) PDF4LHC21 (mc23)	PYTHIA8 A14	FS AF3	
	POWHEGBOX v2	NLO	NNPDF3.0nlo	HERWIG7 H7.2-Default	FS	
$t\bar{t}Z$	MADGRAPH5_AMC@NLO NLO		NNPDF3.0 NNLO	PYTHIA8 A14	FS	
$t\bar{t}W$	SHERPA	NLO	NNPDF3.0 NNLO	SHERPA SHERPA	FS	
	SHERPA	LO	NNPDF3.0 NNLO	SHERPA SHERPA	FS	
$t\bar{t}$ and Single-Top						
$t\bar{t}$	POWHEGBOX v2	NLO	NNPDF3.0nlo	PYTHIA8 A14	FS	
tW	POWHEGBOX v2	NLO	NNPDF3.0nlo	PYTHIA8 A14	FS	
$t(q)b$	POWHEGBOX v2	NLO	NNPDF3.0nlo (s) NNPDF3.0nlo 4f (t)	PYTHIA8 A14	FS FS	
tWZ	MADGRAPH5_AMC@NLO NLO		NNPDF3.0nlo	PYTHIA8 A14	FS	
tZ	MADGRAPH5_AMC@NLO LO		NNPDF3.0nlo 4f	PYTHIA8 A14	FS	
$t\bar{t}VV$						
$t\bar{t}WW$	MADGRAPH5_AMC@NLO LO (mc20)		NNPDF3.0nlo	PYTHIA8 A14	FS	
	MADGRAPH (mc23)				FS	
$t\bar{t}WZ$	MADGRAPH	LO	NNPDF3.0nlo	PYTHIA8 A14	AF3	
$t\bar{t}HH$	MADGRAPH	LO	NNPDF3.0nlo	PYTHIA8 A14	AF3	
$t\bar{t}WH$	MADGRAPH	LO	NNPDF3.0nlo	PYTHIA8 A14	AF3	
$t\bar{t}ZZ$	MADGRAPH	LO	NNPDF3.0nlo	PYTHIA8 A14	AF3	
$V(VV)+jets$ and VH						
$V+jets$	SHERPA	NLO	NNPDF3.0 NNLO	SHERPA SHERPA	FS	
$VV+jets$	SHERPA	NLO	NNPDF3.0 NNLO	SHERPA SHERPA	FS	
		LO ($gg \rightarrow VV$)			FS	
$VVV+jets$	SHERPA	NLO	NNPDF3.0 NNLO	SHERPA SHERPA	FS	
VH	POWHEGBOX v2	NLO	NNPDF3.0 AZNLO	PYTHIA8 A14	FS	

948 **Chapter 6. Analysis Strategy**

949 **6.1 Event selection**

950 Events for the analysis first are preselected following a list of criteria to optimize for event
951 quality and background rejection.

952 The criteria are applied sequentially, from top to bottom

953 1. **Good Run List (GRL)**: data events must be part of a predefined list of suitable
954 runs and luminosity blocks.

955 2. **Calorimeter cleaning**: events containing signal hits indicating an error in the calorime-
956 ter are removed.

957 3. **Primary vertex**: events must have at least one reconstructed vertex matched to 2 or
958 more associated tracks with $p_T > 500$ MeV.

959 4. **Trigger**: events must be selected by at least one trigger documented in ??.

960 5. **Jet cleaning**: events must pass the LooseBad WP for jet cleaning using jets passing
961 preselection criteria in section 4.6. This is done to remove events with significant
962 number of calorimeter hits from non-prompt sources (e.g. instrumental effects, cosmic
963 ray background, non-collision particles)

964 6. **Bad muon veto**: events are removed if they contain at least one muon before overlap
965 removal with insufficient p_T resolution.

966 7. **Kinematic selection**: events must have exactly two Tight leptons with the same
967 electric charge, or at lease three Tight leptons of any charge. The leading lepton must

968 have $p_T > 28$ GeV, and all leptons must satisfy $p_T > 15$ GeV.

969 Events are separated into two channels based on the number of leptons: same-sign di-lepton
970 (SS2L) for events with exactly two leptons of the same charge, or multilepton (ML) for
971 events with three or more leptons. The channels are further separated into regions defined
972 in section 6.2 to prepare for analysis.

973 Further selections are applied based on the lepton flavors present. In the SS2L channel, if
974 both leptons are electrons, the invariant mass m_{ll} must satisfy $m_{ll} < 81$ GeV and $m_{ll} > 101$
975 GeV to suppress background involving Z -bosons. In the ML channel, the same criteria must
976 be satisfied for every opposite-sign same-flavor pair of leptons in an event.

977 Event categorization

978 Simulated events are categorized using truth information of leptons (e/μ) and their origi-
979 nating MC particle (mother-particle).

980 Each lepton can be classified as either prompt or non-prompt, with non-prompt leptons fur-
981 ther categorized for background estimation purposes.

982 If an event contains only prompt leptons, the event is classified as its corresponding process.
983 If the event contains one non-prompt lepton, the event is classified as the corresponding type
984 of the non-prompt lepton. If the event contains more than one non-prompt lepton, the event
985 is classified as other.

986 • **Prompt:** if the lepton originates from $W/Z/H$ boson decays, or from a mother-
987 particle created by a final state photon.

988 • **Non-prompt:**

- **Charge-flip (e only)**: if the reconstructed charge of the lepton differs from that of the first mother-particle.
- **Material conversion (e only)**: if the lepton originated from a photon conversion and the mother-particle is an isolated prompt photon, non-isolated final state photon, or heavy boson.
- **γ -conversion (e only)**: if the lepton originated from a photon conversion and the mother-particle is a background electron.
- **Heavy flavor decay**: if the lepton originated from a b - or c -hadron.
- **Fake**: if the lepton originated from a light- or s -hadron, or if the truth type of the lepton is hadron.
- **Other**: any lepton that does not belong to one of the above categories.

6.2 Analysis regions

Events are selected and categorized into analysis regions belonging to one of two types: control regions (CRs) enriched in background events, and signal regions (SRs) enriched in signal events. This allows for the examination and control of backgrounds and systematic uncertainties, as well as study of signal sensitivities.

The signal is then extracted from the SRs with a profile LH fit using all regions. The full selection criteria for each region are summarized in Table 6.3

6.2.1 Signal regions

- All events selected for SS2L and 3L signal regions must satisfy the following criteria:

- 1009 • Contains 6 or more jets, with at least 2 jets b -tagged at the 85% WP
- 1010 • Scalar sum of the transverse momenta of all leptons and jets $H_T > 500$ GeV
- 1011 • Dilepton invariant mass $m_{\ell\ell}$ does not coincide with the Z -boson mass range of $81 - 101$
- 1012 GeV
- 1013 - The SR is further granularized by the number of b -jets and leptons to further study and
- 1014 improve signal sensitivity

1015

Table 6.1: Caption

SR	Selection criteria	
	b -jets	leptons
2b2l	$N_b = 2$	$N_l = 2$
2b3l4l	$N_b = 2$	$N_l \geq 3$
3b2l	$N_b = 3$	$N_l = 2$
3b3l4l	$N_b = 3$	$N_l \geq 3$
4b	$N_b = 4$	

1016 6.2.2 Control regions

- 1017 Control regions are defined for each background to be enriched in the targeted background
- 1018 events, in order to maximize the targeted background's purity and minimize contamination
- 1019 from other sources within the region.
- 1020 This helps to constrain and reduce correlation between background normalization factors.
- 1021 Fit variables and selection criteria are determined via optimization studies on CRs to achieve
- 1022 the largest discriminating power possible between the target background and other event
- 1023 types.

1024 **$t\bar{t}W$ background CRs**

1025 Two types of CRs are defined to estimate the flavor composition and normalization of $t\bar{t}W$
1026 +jets background: CR $t\bar{t}W^\pm$ +jets to constrain flavor composition, and CR 1b(\pm) to con-
1027 strain jet multiplicity spectrum.
1028 These are further split into CR $t\bar{t}W^\pm$ and CR 1b(\pm) due to the pronounced asymmetry in
1029 $t\bar{t}W$ production from pp collisions, with $t\bar{t}W^+$ being produced at approximately twice the
1030 rate of $t\bar{t}W^-$. Selections on H_T and N_{jets} to ensure orthogonality to SR
1031 Selections on total charge for each charged W^\pm boson

1032

1033 **Fake/non-prompt background CRs**

1034 Selection for fake/non-prompt CRs are determined using the `DFCommonAddAmbiguity` (DF-
1035 CAA) variable for reconstructed leptons.

Table 6.2: Caption

DFCAA	Description
-1	No 2nd track found
0	2nd track found, no conversion found
1	Virtual photon conversion candidate
2	Material conversion candidate

1036 Four CRs for three main types of fake/non-prompt backgrounds: virtual photon (γ^*)
1037 conversion, photon conversion in detector material (Mat. Conv.) and heavy flavor decays
1038 (HF).

1039

- 1040 • Low m_γ^* : events with an e^+e^- pair produced from a virtual photon

- 1041 Selects two same-sign leptons with at least one electron reconstructed as an internal
 1042 conversion candidate and neither as with a material conversion candidate ($\text{DFCAA}_{\ell_1(\ell_2)} =$
 1043 1 and $\neq 2$)
 1044 NF constrained using yield count only.
 1045 • Mat. Conv.: events with an electron originating from photon conversion within the
 1046 detector material.
 1047 Selects two same-sign leptons with at least one electron reconstructed as a material
 1048 conversion candidate ($\text{DFCAA}_{\ell_1(\ell_2)} = 2$).
 1049 NF constrained using yield count only.
 1050 • HF e/μ : events with a reconstructed non-prompt lepton from semi-leptonic decays of
 1051 b - and c -hadrons (heavy flavor decays)
 1052 Selects three leptons with at least two electrons/muons, with no lepton reconstructed
 1053 as a conversion candidate ($\text{DFCAA} < 0$).
 1054 NFs constrained by fitting with p_T of the third leading lepton ℓ_3 .

1055 6.2.3 Validation regions

- 1056 In addition, validation regions are also defined to validate the normalization and modeling
 1057 of $t\bar{t}Z$ and $t\bar{t}W$ background without being used in the fit.
 1058 • $t\bar{t}Z$: Selects events with at least two b -tagged jets, at least four total jets and three
 1059 leptons with at least one same-flavor opposite-sign lepton pair possessing invariant
 1060 mass $m_{\ell\ell}$ within the Z -boson mass window of $81 - 101$ GeV
 1061 • $t\bar{t}W$: Main charge asymmetric background leaning $t\bar{t}W^+$, validated using the difference
 1062 in number of positively and negatively charged events $N_+ - N_-$ instead of total number

1063 of events.

1064 Selects using CR $t\bar{t}W$ and CR 1b criteria, with one VR not orthogonal to SR and one
1065 orthogonal VR with more limited statistics.

Table 6.3: Caption

Region	Channel	N_{jets}	N_b	Other selections	Fitted variable
CR Low m_{γ^*}	SS $e\ell$	[4, 6)	≥ 1	ℓ_1/ℓ_2 is from virtual photon decay $\ell_1 + \ell_2$ not from material conversion	event yield
CR Mat. Conv.	SS $e\ell$	[4, 6)	≥ 1	ℓ_1/ℓ_2 is from material conversion $\ell_1 + \ell_2$ not conversion candidates	event yield
CR HF μ	$\ell\mu\mu$	≥ 1	1	$100 < H_T < 300 \text{ GeV}$ $E_T^{\text{miss}} > 35 \text{ GeV}$ total charge = ± 1	$p_T(\ell_3)$
CR HF e	$e\ell\ell$	≥ 1	1	$\ell_1 + \ell_2$ not conversion candidates $100 < H_T < 275 \text{ GeV}$ $E_T^{\text{miss}} > 35 \text{ GeV}$ total charge = ± 1	$p_T(\ell_3)$
CR $t\bar{t}W^+$	SS $\ell\mu$	≥ 4	≥ 2	$ \eta(e) < 1.5$ for $N_b = 2$: $H_T < 500 \text{ GeV}$ or $N_{\text{jets}} < 6$ for $N_b \geq 3$: $H_T < 500 \text{ GeV}$ total charge > 0	N_{jets}
CR $t\bar{t}W^-$	SS $\ell\mu$	≥ 4	≥ 2	$ \eta(e) < 1.5$ for $N_b = 2$: $H_T < 500 \text{ GeV}$ or $N_{\text{jets}} < 6$ for $N_b \geq 3$: $H_T < 500 \text{ GeV}$ total charge < 0	N_{jets}
CR 1b(+)	SS2L+3L	≥ 4	1	$\ell_1 + \ell_2$ not from material conversion $H_T > 500 \text{ GeV}$ total charge > 0	N_{jets}
CR 1b(-)	SS2L+3L	≥ 4	1	$\ell_1 + \ell_2$ not from material conversion $H_T > 500 \text{ GeV}$ total charge < 0	N_{jets}
VR $t\bar{t}Z$	3L $\ell^\pm\ell^\mp$	≥ 4	≥ 2	$m_{\ell\ell} \in [81, 101] \text{ GeV}$	$N_{\text{jets}}, m_{\ell\ell}$
VR $t\bar{t}W +1b$	SS2L+3L			CR $t\bar{t}W^\pm$ CR 1b(\pm)	N_{jets}
VR $t\bar{t}W +1b+SR$	SS2L+3L			CR $t\bar{t}W^\pm$ CR 1b(\pm) SR	N_{jets}
SR	SS2L+3L	≥ 6	≥ 2	$H_T > 500 \text{ GeV}$ $m_{\ell\ell} \notin [81, 101] \text{ GeV}$	H_T

1066 **6.3 Background estimation**

1067 Background events in this analysis consist of SM processes that can result in a $t\bar{t}t\bar{t}$ SSML

1068 final state.

1069 Can be divided into two types: reducible and irreducible.

1070 Reducible background consists of processes that do not result in SSML final state physically,

1071 but are reconstructed as such due to erroneous detector and reconstruction effects.

1072 Three main types: charge misidentification (QmisID), fake leptons and non-prompt leptons.

1073 Estimated using template fitting method to adjust MC predictions via floating normalization

1074 factors constrained in the CRs.

1075 Irreducible background consists of SM processes that result in SSML final states physically,

1076 with all leptons being prompt.

1077 Main irreducible background considered in this analysis: $t\bar{t}t\bar{t}$, $t\bar{t}W$, $t\bar{t}Z$, and $t\bar{t}H$ with smaller

1078 contributions from VV , VVV , VH and rarer processes like $t\bar{t}VV$, tWZ , tZq and $t\bar{t}t$.

1079 Most irreducible backgrounds are estimated using MC simulations normalized to their the-

1080 oretical SM cross sections (template fitting), with the exception of $t\bar{t}W$ background due to

1081 MC mismodeling of the process at high jet multiplicities.

1082 The $t\bar{t}W$ is instead given four dedicated CRs, and estimated using a data-driven method

1083 with a fitted function parameterized in N_{jets}

1084 All CRs and SR are included in the final LH-fit to data.

1085 **6.3.1 Template fitting for fake/non-prompt estimation**

1086 Template fit method is a semi-data-driven approach that estimates fake/non-prompt back-

1087 ground distributions by fitting the MC kinematic profiles of background processes arising

1088 from fake/non-prompt leptons to data.

1089 Each of the four main sources of fake/non-prompt leptons is assigned a free-floating normal-

1090 ization factor constrained by a CR enriched with the corresponding background. The NFs

1091 are determined simultaneously with the signal.

1092 • $\text{NF}_{\text{HF } e(\mu)}$: events with one reconstructed non-prompt electron (muon) from heavy

1093 flavor decays,

1094 • $\text{NF}_{\text{Mat. Conv.}}$: events with one reconstructed non-prompt electrons from photon con-

1095 version in the detector material

1096 • $\text{NF}_{\text{Low } m_{\gamma^*}}$: events with one reconstructed non-prompt electrons in an e^+e^- pair from

1097 virtual photon (γ^*) conversion.

1098 6.3.2 Charge misidentification data-driven estimation

1099 The same-sign di-lepton channel in the analysis gives rise to a major background contami-

1100 nation in opposite-sign di-lepton events with one misidentified charge.

1101 Charge misidentification occurs via incorrect track curvature measurements or trident elec-

1102 tron contamination from bremsstrahlung, and therefore mainly concerns electrons due to

1103 muons' low bremsstrahlung rate and precise curvature information using the ID and MS.

1104 The charge misidentification rates is significant at higher p_T and varies with $|\eta|$ as a proxy for

1105 the amount of detector material the electron interacted with, and is consequently estimated

1106 in this analysis using a data-driven method with assistance from ECIDS.

1107 The charge flip probability ϵ is estimated using a sample of $Z \rightarrow e^+e^-$ events with additional

1108 constraints on the invariant mass m_{ee} to be within 10 GeV of the Z -boson mass.

1109 The Z -boson mass window is defined to be within 4σ to include most events within the peak,

1110 and is determined by fitting the m_{ee} spectrum of the two leading electrons to a Breit-Wigner
1111 function, resulting in a range of [65.57, 113.49] for SS events and [71.81, 109.89] for OS events.

1112 Background contamination near the peak is assumed to be uniform and subtracted using a
1113 sideband method.

1114 Since the Z -boson decay products consist of a pair of opposite-sign electrons, all same-sign
1115 electron pairs are considered to be affected by charge misidentification.

1116 Assuming the charge flip probabilities of electrons in an event are uncorrelated, the number
1117 of events with same-sign electrons N_{ij}^{SS} with the leading electron in the i^{th} 2D bin in $(p_T, |\eta|)$
1118 and the sub-leading electron in the j^{th} bin can be estimated as

$$N_{ij}^{\text{SS}} = N_{ij}^{\text{tot}}(\epsilon_i(1 - \epsilon_j) + \epsilon_j(1 - \epsilon_i)), \quad (6.1)$$

where N_{ij}^{tot} is the total number of events in the i^{th} and j^{th} bin regardless of charge, and $\epsilon_{i(j)}$ is the charge flip rate in the $i^{\text{th}}(j^{\text{th}})$ bin.

Assuming N_{ij}^{SS} follows a Poisson distribution around the expectation value \bar{N}_{ij}^{SS} , the charge flip rate ϵ can be estimated by minimizing a negative-LLH function parameterized in p_T and $|\eta|$,

$$-\ln(\mathcal{L}(\epsilon | N_{\text{SS}})) = -\ln \prod_{ij} \frac{(N_{ij}^{\text{tot}})^{N_{ij}^{\text{SS}}} \cdot e^{N_{ij}^{\text{tot}}}}{N_{ij}^{\text{SS}}!} \quad (6.2)$$

$$= - \sum_{ij} \left[N_{ij}^{\text{SS}} \ln(N_{ij}^{\text{tot}}(\epsilon_i(1 - \epsilon_j) + \epsilon_j(1 - \epsilon_i))) - N_{ij}^{\text{tot}}(\epsilon_i(1 - \epsilon_j) + \epsilon_j(1 - \epsilon_i)) \right]. \quad (6.3)$$

1119 The charge flip rate is then calculated separately for SR and CRs with different electron
 1120 definitions (CR Low m_{γ^*} , CR Mat. Conv., CR $t\bar{t}W$) using events satisfying 2LSS kinematic
 1121 selections but with OS electrons, after applying region-specific lepton selections and ECIDS.
 1122 The following weight is applied to OS events to correct for misidentified SS events within
 1123 the region:

$$w = \frac{\epsilon_i + \epsilon_j - 2\epsilon_i\epsilon_j}{1 - \epsilon_i - \epsilon_j + 2\epsilon_i\epsilon_j}. \quad (6.4)$$

1124 6.3.3 $t\bar{t}W$ background data-driven estimation

1125 - $t\bar{t}W$ represents a major source of irreducible background contamination in SM and BSM
 1126 analyses with $t\bar{t}t\bar{t}$ final states.

1127 - Measured cross section for $t\bar{t}W$ background has been consistently higher than predicted
 1128 values as seen in previous analyses ($t\bar{t}H/t\bar{t}W$ multilepton [39][40], $t\bar{t}t\bar{t}$ analyses [41][42]) due
 1129 to mismodeling, especially at higher N_{jets}
 1130 (show postfit $t\bar{t}W$ VR distribution)

1131 - Previously, this was handled by assigning large ad-hoc systematic uncertainties to $t\bar{t}W$
 1132 events with 7 or more jets. - A semi-data-driven method originally employed in the R-parity-
 1133 violating-supersymmetry search [43] was used to mitigate this problem. - This method was
 1134 shown to be effective in the SM $t\bar{t}t\bar{t}$ observation analysis [[ana:tttt::obs](#)] by improving $t\bar{t}W$
 1135 modeling especially in the showering step and switching $t\bar{t}W$ systematic uncertainties from
 1136 predominantly modeling to statistical.

1137 - MC kinematic distributions for $t\bar{t}W$ are applied with correction factors obtained from a
 1138 fitted function parameterized in N_{jets} .

1139 - The function describes scaling patterns for QCD [44] can be represented by ratio of suc-

₁₁₄₀ cessive exclusive jet cross-sections

$$R_{(n+1)/n} = e^{-b} + \frac{\bar{n}}{n+1} = a_0 + \frac{a_1}{1+(j-4)}, \quad (6.5)$$

₁₁₄₁ where n is the number of jets in addition to the hard process, j is the inclusive number of
₁₁₄₂ jets, and \bar{n} is the expectation value for the Poisson distribution for exclusive jet cross-section
₁₁₄₃ at jet multiplicity n , described as $P_n = \sigma_n / \sigma_{\text{tot}}$.

₁₁₄₄ - Same-sign di-lepton $t\bar{t}W$ events dominate the $t\bar{t}W$ background and produce 4 jets in the
₁₁₄₅ matrix element at tree level for the hard process, so n is defined starting from 5 jets and j
₁₁₄₆ is defined as inclusive number of jets with 4 or more jets, or $j \equiv n + 4$.

₁₁₄₇ - The two terms in the equation correspond respectively to staircase and Poisson scaling
₁₁₄₈ between successive multiplicity cross sections, defined as constant ratios e^{-b} and ratios be-
₁₁₄₉ tween Poisson probability for $n+1$ and n jets. Staircase scaling is sensitive to events with
₁₁₅₀ high jet multiplicity, while Poisson scaling is sensitive to events with low jet multiplicity [44].

₁₁₅₁ - The scaling pattern can then be re-parameterized in a_0 and a_1 to obtain the $t\bar{t}W$ yield at
₁₁₅₂ j'

$$\text{Yield}_{t\bar{t}W(j')} = \text{Yield}_{t\bar{t}W(j=4)} \times \prod_{j=4}^{j'-1} \left(a_0 + \frac{a_1}{1+(j-4)} \right) \quad (6.6)$$

₁₁₅₃ where j' is defined as $j' \equiv j+1$ with $j \geq 4$ since the parameterization starts at the 4th jet.

₁₁₅₄ The $t\bar{t}W$ yield at the 4-jet bin can be represented by a normalization factor applied to $t\bar{t}W$

₁₁₅₅ MC simulation as $\text{Yield}_{t\bar{t}W(j=4)} = \text{NF}_{t\bar{t}W(j=4)} \times \text{MC}_{j=4}$.

₁₁₅₆ To account for the disparity in $t\bar{t}W^+$ and $t\bar{t}W^-$ cross-section, assuming the scaling is the
₁₁₅₇ same for both processes, $\text{NF}_{t\bar{t}W(j=4)}$ can be further split into $\text{NF}_{t\bar{t}W^+(j=4)}$ and $\text{NF}_{t\bar{t}W^-(j=4)}$.

₁₁₅₈ Both NFs are left free-floating to constrain $t\bar{t}W$ yields at the 4-jet bin in CR 1b(+) and CR

₁₁₅₉ 1b(-).

₁₁₆₀ The final N_{jets} -parameterized function can then be represented by $\text{NF}_{t\bar{t}W(j')}$ as

$$\text{NF}_{t\bar{t}W(j')} = \left(\text{NF}_{t\bar{t}W^+(j=4)} + \text{NF}_{t\bar{t}W^-(j=4)} \right) \times \prod_{j=4}^{j'-1} \left(a_0 + \frac{a_1}{1+(j-4)} \right). \quad (6.7)$$

₁₁₆₁ This normalization is calculated and applied separately for each sub-sample of $t\bar{t}W^+$ and
₁₁₆₂ $t\bar{t}W^-$ in an N_{jets} bin for $4 \leq N_{\text{jets}} < 10$.

₁₁₆₃ Due to small contributions in the CRs, events with $N_{\text{jets}} < 4$ and $N_{\text{jets}} \geq 10$ are not
₁₁₆₄ normalized with this scheme.

₁₁₆₅ Instead, $N_{\text{jets}} < 4$ $t\bar{t}W$ events are fitted by propagating normalization in the 4-jet bin
₁₁₆₆ without additional shape correction. The correction factor for $t\bar{t}W$ events with $N_{\text{jets}} \geq$
₁₁₆₇ 10 is obtained by summing up the overflow from $N_{\text{jets}} = 10$ to $N_{\text{jets}} = 12$, described as
₁₁₆₈ $\sum_{j'=10}^{12} \prod_{j=4}^{j'-1} \left(a_0 + \frac{a_1}{1+(j-4)} \right)$. Events with $N_{\text{jets}} \geq 13$ are negligible and thus not included
₁₁₆₉ in the sum.

₁₁₇₀ Control region definitions

₁₁₇₁ Four control regions CR $t\bar{t}W^+$, CR $t\bar{t}W^-$, CR 1b(+), CR 1b(-) are constructed to fit
₁₁₇₂ $\text{NF}_{t\bar{t}W^\pm(j=4)}$ and the scaling parameters a_0 , a_1 for the $t\bar{t}W$ background, as well as vali-
₁₁₇₃ dating the parameterization.

₁₁₇₄ Events in CR $t\bar{t}W^\pm$ are required to contain at least two b -tagged jets similar to the SR to
₁₁₇₅ determine the $t\bar{t}W$ normalization within an SR-related phase space. Orthogonality with SR
₁₁₇₆ is satisfied by requiring $H_T < 500$ GeV or $N_{\text{jets}} < 6$ when $N_b = 2$, and $H_T < 500$ GeV when
₁₁₇₇ $N_b \geq 3$.

₁₁₇₈ The remaining CR 1b(\pm) require events to have $H_T > 500$ GeV and at least four jets to

1179 encompass events with high N_{jets} , which can be used to determine the $t\bar{t}W$ jet multiplicity spectrum for fitting $a_{0,1}$. The selection criteria also include exactly one b -tagged jet to
1180 maintain orthogonality with SR. Assuming the $t\bar{t}W$ jet multiplicity distribution is similar
1181 across different N_b , a fitted N_{jets} distribution in CR 1b(\pm) can be used to describe the $t\bar{t}W$
1182 parameterization at higher N_{jets} . The full selection criteria for all four regions are shown in
1183
1184 ??

1185

1186 Validating the $t\bar{t}W$ parameterization in Equation 6.7 makes use of the unique charge
1187 asymmetry in $t\bar{t}W$ production that's not present in other background or signal processes.
1188 The number of events with all negatively charged leptons is subtracted from that of events
1189 with all positively charged leptons, which cancels out charge symmetric events and leaves
1190 the $t\bar{t}W$ background. Validation is done via a statistical-only (stat-only) fit to the $t\bar{t}W$ MC
1191 prediction in CR 1b(\pm).
1192

1192 Chapter 7. Systematic Uncertainties

1193 (nuisance parameters)

1194 - Heavy pruning, 5% on shape and normalization pruning (to fit timeline?)

1195 7.1 Experimental uncertainties

1196 Instrumental & minor:

1197 - uncertainty on the integrated luminosity of the 2015-2018 Run 2 data set is 0.83%, obtained

1198 by the LUCID-2 detector for the primary luminosity measurements complemeted by the ID

1199 and calorimeters

1200 - Pile-up modeling in MC was calibrated to data through pile-up reweighting, resulting in a
1201 set of calibration SFs and associated uncertainties.

1202 In general, calibrating MC simulations to match performance in data incurs uncertainties

1203 associated with the MC-to-data scale factors obtained from the calibration, which are in

1204 turn propagated to observables in the analysis.

1205 7.1.1 Leptons

1206 The trigger/reconstruction/ID/isolation efficiencies of electrons and muons (with separate
1207 systematic and statistical components for muon) differ between MC simulation and data,
1208 and require correction in the form of SFs with its associated uncertainties.

1209 Similarly, electron and muon energy-momentum scale and resolution also incur uncertainties
1210 from MC-to-data correction, calculated by varying scale and resolution during simulations.

1211 Muons have additional uncertainties for charge-dependent and charge-independent momen-

1212 tum scale, and detector-specific (ID, MS, CB) track resolution.

1213 The charge identification/ECIDS efficiency also gives rise to an additional uncertainty com-

1214 ponent.

1215

1216 7.1.2 Jets

1217 Experimental uncertainties on jets are dominated by flavor tagging-related uncertainties,

1218 with subleading contributions from jet energy scale/resolution (JES/JER) and NNJvt cali-

1219 bration.

1220

1221 Jet energy scale

1222 JES and its associated uncertainties are determined using data from test-beam and LHC

1223 collisions and MC simulated samples, decomposed into uncorrelated components:

- 1224 • Effective nuisance parameters (NPs): 15 p_T -dependent uncertainty components in total
1225 measured in situ, grouped based on their origin (2 detector-related, 4 modeling-related,
1226 3 mixed, 6 statistical-related)

- 1227 • η intercalibration: 6 total components (1 modeling-related, 4 non-closure and 1 statistical-
1228 related) associated with the correction of the forward jets' ($0.8 \leq |\eta| < 4.5$) energy
1229 scale to that of the central jets ($|\eta| < 0.8$).

- 1230 • Flavor composition/response: 2 components for relative quark-gluon flavor composi-
1231 tions in background and signal samples, and 2 components for uncertainty in responses
1232 to gluon-initiated versus quark-initiated jets

- Pile-up subtraction: 4 components, two for uncertainty in μ (`OffsetMu`) and N_{PV} (`OffsetNPV`) modeling, one for residual p_T -dependency (`PtTerm`) and one for topology dependence on the per-event p_T density modeling (`RhoTopology`)
- Punch-through effect treatment: two terms (AF3 fast simulation and full detector simulations) for GSC punch-through jet response correction between data and MC.
- Non-closure: one term to account for difference between AF3-simulated samples and full detector simulations.
- High- p_T single-particle response: one term for response to high- p_T jets from single-particle and test-beam measurements
- b -jets response: one term for uncertainty in the response to b -jets

1243 Jet energy resolution

1244 JER measured separately in data and MC simulations using in situ techniques as a function
 1245 of p_T and η for a given jet. Associated uncertainties are defined as quadratic difference
 1246 between data and MC simulations.
 1247 This analysis uses the full JER uncertainty set provided for Run 2 searches with 14 total com-
 1248 ponents: 12 effective NPs and 2 for difference between data and MC simulation, separately
 1249 for AF3 and FS.

1250 Jet vertex tagging

1251 JVT associated uncertainty is obtained by varying the JVT efficiency correction SFs within
 1252 their range of uncertainty. This uncertainty accounts for remaining contamination from
 1253 pile-up jets after applying pile-up suppression and MC generator choice.

1254 **Flavor tagging**

1255 SFs for b -jets tagging efficiencies and c -/light-jets mis-tagging rates are obtained as a function
1256 of p_T for b -/ c -/light-jets and PCB scores. The covariance matrix of systematic and statistical
1257 uncertainties is diagonalized and reduced in dimensions using principle component analysis
1258 (PCA), resulting in a set of orthogonal NPs: 85 for b -jets, 56 for c -jets and 42 for light-jets.

1259 **7.1.3 Missing transverse energy**

1260 Uncertainties for E_T^{miss} arise from possible miscalibration of its soft-track component, and
1261 are estimated using data-MC comparison of the p_T scale and resolution between the hard
1262 and soft E_T^{miss} terms. These uncertainties are represented by three independent terms: one
1263 for scale uncertainty and two resolution uncertainties for the parallel and perpendicular
1264 components.

1265 **7.2 Modeling uncertainties**

1266 **7.2.1 Signal and irreducible background uncertainties**

1267 - scale variations - 6-point variation method, varying μ_R & μ_F vs central values to cover
1268 missing higher-order QCD corrections (signal & all major irreducible background)
1269 $(\mu_R, \mu_F) = (0.5, 0.5), (0.5, 1), (1, 0.5), (1, 2), (2, 1), (2, 2)$ - pdf uncertainty: flat 1% for $t\bar{t}Z'$,
1270 $t\bar{t}t\bar{t}$, $t\bar{t}Z$, $t\bar{t}H$, envelope of differences between nominal vs. other pdf choices for $t\bar{t}t$

1271 **$t\bar{t}Z'$ signal**

1272 - parton distribution function: 1%

Table 7.1: Summary of the experimental systematic uncertainties considered in this analysis.

Systematic uncertainty	Terms	Scale [%]
Event		
Luminosity	1	0.83
Pile-up reweighting	1	$\mathcal{O}(1) \sim \mathcal{O}(10)$
Electrons		
Trigger efficiency	1	$\mathcal{O}(10^{-2}) \sim \mathcal{O}(10^{-1})$
Reconstruction efficiency [†]	1	$\mathcal{O}(10^{-1}) \sim \mathcal{O}(1)$
Identification efficiency [†]	1	$\mathcal{O}(10^{-1}) \sim \mathcal{O}(1)$
Isolation efficiency [†]	1	$\mathcal{O}(10^{-1}) \sim \mathcal{O}(1)$
Energy scale	1	$\mathcal{O}(10^{-2}) \sim \mathcal{O}(10^{-1})$
Energy resolution	1	$\mathcal{O}(10^{-2}) \sim \mathcal{O}(10^{-1})$
Charge identification (ECIDS) efficiency [†]	1	$\mathcal{O}(10^{-1}) \sim \mathcal{O}(1)$
Muons		
Trigger efficiency (stat/sys)	2	$\mathcal{O}(10^{-1}) \sim \mathcal{O}(1)$
Track-to-vertex association efficiency (stat/sys)	2	$\mathcal{O}(10^{-2}) \sim \mathcal{O}(10^{-1})$
Reconstruction/identification efficiency (stat/sys)	2	$\mathcal{O}(10^{-1}) \sim \mathcal{O}(1)$
Low- p_T (< 15 GeV) reconstruction/identification efficiency (stat/sys)	2	$\mathcal{O}(10^{-1}) \sim \mathcal{O}(1)$
Isolation efficiency (stat/sys)	2	$\mathcal{O}(10^{-1}) \sim \mathcal{O}(1)$
Charge-independent momentum scale	1	$\mathcal{O}(10^{-2}) \sim \mathcal{O}(10^{-1})$
Charge-dependent momentum scale	4	$\mathcal{O}(10^{-2}) \sim \mathcal{O}(10^{-1})$
Energy resolution (CB)	1	$\mathcal{O}(10^{-2}) \sim \mathcal{O}(10^{-1})$
Energy resolution (ID & MS)*	2	$\mathcal{O}(10^{-2}) \sim \mathcal{O}(10^{-1})$
Jets		
JES effective NP	15	$\mathcal{O}(10^{-2}) \sim \mathcal{O}(1)$
JES η intercalibration	3	$\mathcal{O}(10^{-1}) \sim \mathcal{O}(1)$
JES flavor composition	2	$\mathcal{O}(10^{-1}) \sim \mathcal{O}(1)$
JES flavor response	1	$\mathcal{O}(10^{-1}) \sim \mathcal{O}(1)$
JES pile-up	4	$\mathcal{O}(10^{-1}) \sim \mathcal{O}(10)$
JES punch-through (FS/AF3*)	2	$< \mathcal{O}(10^{-2})$
JES non-closure	1	$\mathcal{O}(10^{-2}) \sim \mathcal{O}(10^{-1})$
JES high- p_T single particle	1	$< \mathcal{O}(10^{-2})$
JES b -jet response	1	$\mathcal{O}(10^{-1}) \sim \mathcal{O}(1)$
JER effective NP	12	$\mathcal{O}(10^{-1}) \sim \mathcal{O}(1)$
JER data/MC (FS/AF3*)	2	$\mathcal{O}(10^{-1}) \sim \mathcal{O}(1)$
JVT efficiency	1	$\mathcal{O}(10^{-1}) \sim \mathcal{O}(1)$
GN2v01 b -tagging efficiency (b -jets)	85	$\mathcal{O}(10^{-2}) \sim \mathcal{O}(1)$
GN2v01 b -tagging efficiency (c -jets)	56	$\mathcal{O}(10^{-2}) \sim \mathcal{O}(1)$
GN2v01 b -tagging efficiency (light-jets)	42	$\mathcal{O}(10^{-2}) \sim \mathcal{O}(1)$
E_T^{miss}-Terms		
Track-based soft term for transversal resolution	1	$\mathcal{O}(10^{-2}) \sim \mathcal{O}(10^{-1})$
Track-based soft term for longitudinal resolution	1	$\mathcal{O}(10^{-2}) \sim \mathcal{O}(10^{-1})$
Track-based soft term for longitudinal scale	1	$\mathcal{O}(10^{-2}) \sim \mathcal{O}(10^{-1})$

₁₂₇₃ **SM $t\bar{t}t\bar{t}$ background**

₁₂₇₄ - cross section: 20% from NLO prediction in QCD+EW

₁₂₇₅ - generator uncertainty: madgraph5_amc@nlo (nominal) vs sherpa 2.2.10

₁₂₇₆ - parton shower uncertainty: pythia8 (nominal) vs herwig7

₁₂₇₇ **SM $t\bar{t}t$ background**

₁₂₇₈ - cross section: 30% from NLO prediction in QCD+EW

₁₂₇₉ - additional b -jets: 50% for $t\bar{t}t$ events with 4+ truth b -jets

₁₂₈₀ **$t\bar{t}W$, $t\bar{t}Z$, $t\bar{t}H$ background**

₁₂₈₁ - cross section: $t\bar{t}Z$ 12%, $t\bar{t}H$ 10% (**from CERN yellow report**)

₁₂₈₂ no cross-section and pdf uncertainties for $t\bar{t}W$ since normalizations and jet multiplicity spec-

₁₂₈₃ trum are estimated with data-driven method

₁₂₈₄ - parton shower uncertainty: $t\bar{t}H$ powhegbox+pythia8 (nominal) vs powhegbox+herwig7

₁₂₈₅ - additional b -jets: events with additional HF jets can contaminate SR and are challenging

₁₂₈₆ to model w/ MC - 50% for events with an additional truth b -jet not from top-quark decay,

₁₂₈₇ additional 50% for 2 or more

₁₂₈₈ - generator uncertainty **table?**

₁₂₈₉ • $t\bar{t}W$ - sherpa (nominal) vs madgraph5_amc@nlo

₁₂₉₀ • $t\bar{t}Z$ - madgraph5_amc@nlo (nominal) vs sherpa 2.2.10

₁₂₉₁ • $t\bar{t}H$ - powheg8/PhPy8 (nominal) vs powheg8/PhPy8 pthard

₁₂₉₂ **Other backgrounds**

- ₁₂₉₃ • $t(\bar{t})X$: cross section 30%
- ₁₂₉₄ • VV : cross section (STDM-2018-03) uncorrelated 20%/50%/60% for events with 3-
₁₂₉₅ /4/5+ jets; events with 1+ truth b -jets not from top decay 50%
- ₁₂₉₆ • $t\bar{t}VV, VVV, VH$: cross section 50%; additional b -jets same as VV

₁₂₉₇ **7.2.2 Reducible background uncertainties**

- ₁₂₉₈ • Electron charge misidentification background:
- ₁₂₉₉ • Material and internal (low γ^*) conversion background: estimated based on data/MC
₁₃₀₀ differences in a region enriched with $Z \rightarrow \ell^+\ell^-\gamma$; 30% & 21% for material & internal
₁₃₀₁ conversion
- ₁₃₀₂ • Heavy-flavor non-prompt lepton background: estimated based on data/MC differences
₁₃₀₃ in CR/SR distributions, ranging from 20-100%
- ₁₃₀₄ • Light-flavor decays and other fake/non-prompt background: Conservative normal-
₁₃₀₅ ization uncertainty of 100% for light-flavor non-prompt lepton background (ATLAS-
₁₃₀₆ CONF-2019-045), 30% for normalization of all other fake backgrounds.
- ₁₃₀₇ • +HF: contaminates SR phase space with large b -jet multiplicity, estimated
₁₃₀₈ from data/MC discrepancy, 30% for events with

Table 7.2: Caption

Systematic uncertainty	Terms	Scale [%]
$t\bar{t}Z'$ modeling		
Renormalization & factorization scale		
PDF		
SM $t\bar{t}\bar{t}$ modeling		
Cross-section		
Renormalization & factorization scale		
PDF		
Generator choice		
Parton shower model		
SM $t\bar{t}t$ modeling		
Cross-section		
Renormalization & factorization scale		
PDF		
Additional b -jets		
$t\bar{t}W$ modeling		
Renormalization & factorization scale		
Generator choice		
Additional b -jets		
$t\bar{t}Z$ modeling		
Cross-section		
Renormalization & factorization scale		
PDF		
Generator choice		
Additional b -jets		
$t\bar{t}H$ modeling		
Cross-section		
Renormalization & factorization scale		
PDF		
Generator choice		
Parton shower model		
Additional b -jets		
Other background modeling		
Cross-section		
Additional b -jets		

Table 7.3: Caption

Systematic uncertainty	Terms	Scale [%]
Reducible SM background		
$t\bar{t}/V/t+\text{jets}$	2	
Charge misidentification	1	
Fake & non-prompt background		
Low γ^*	1	
Material conversion	1	
HF e	1	
HF μ	1	
Light-flavor decays	1	100
Other fakes	1	30

₁₃₀₉ **Chapter 8. Results**

₁₃₁₀ **8.1 Statistical model**

₁₃₁₁ **8.1.1 Binned profile likelihood fit**

₁₃₁₂ **8.1.2 Signal significance**

₁₃₁₃ **8.1.3 Limit exclusion**

₁₃₁₄ **8.2 Fit results**

₁₃₁₅ Fit setup

- ₁₃₁₆ • Plain Asimov fit (**only mentioning briefly**): all regions included; simulated data used in the fit match exactly to MC prediction with nominal $\mu_{t\bar{t}Z'}$ set to 0 and allowed to free-float.

₁₃₁₉ Purpose: to perform studies on optimizing fitted parameters and expected sensitivity; refining background estimation techniques; optimizing region definition and object definition

- ₁₃₂₂ • Real SRs-blinded fit: similar to plain Asimov, but use observed data in CRs.

₁₃₂₃ Purpose: study the behavior of background estimation using real observed data in CRs on Asimov data in SRs and assessing the influence of statistical effects on fitted parameters and expected sensitivity

- ₁₃₂₆ • Real SRs-unblinded/ H_T fit: all regions included,

₁₃₂₇ **8.3 Limits**

1328 Chapter 9. Summary

1329 References

- 1330 [1] C. Burgard and D. Galbraith. *Standard Model of Physics*. URL: [https://texample.net/
model-physics/](https://texample.net/model-physics/) (visited on 06/02/2025) (cit. on p. 4).
- 1331 [2] A. Pich. *The Standard Model of electroweak interactions. 2004 European School of
High-Energy Physics*. Feb. 2005, pp. 1–48. arXiv: [hep-ph/0502010 \[hep-ex\]](https://arxiv.org/abs/hep-ph/0502010) (cit. on
p. 13).
- 1332 [3] P. Higgs. *Broken symmetries and the masses of gauge bosons*. *Phys. Rev. Lett.* **13** (16
1333 1964), pp. 508–509 (cit. on p. 13).
- 1334 [4] P. Higgs. *Broken symmetries, massless particles and gauge fields*. *Physics Letters* **12.2**
1335 (1964), pp. 132–133. ISSN: 0031-9163 (cit. on p. 13).
- 1336 [5] F. Englert and R. Brout. *Broken Symmetry and the Mass of Gauge Vector Mesons*.
1337 *Phys. Rev. Lett.* **13** (9 1964), pp. 321–323 (cit. on p. 13).
- 1338 [6] ATLAS Collaboration. *Observation of a new particle in the search for the Standard
Model Higgs boson with the ATLAS detector at the LHC*. *Phys. Lett. B* **716** (2012),
1339 p. 1. arXiv: [1207.7214 \[hep-ex\]](https://arxiv.org/abs/1207.7214) (cit. on p. 14).
- 1340
- 1341
- 1342
- 1343

- 1344 [7] CMS Collaboration. *Observation of a new boson at a mass of 125 GeV with the CMS*
1345 *experiment at the LHC*. *Phys. Lett. B* **716** (2012), p. 30. arXiv: [1207.7235 \[hep-ex\]](#)
1346 (cit. on p. 14).
- 1347 [8] J. Ellis. *Higgs Physics. 2013 European School of High-Energy Physics*. 2015, pp. 117–
1348 168. arXiv: [1312.5672 \[hep-ph\]](#) (cit. on pp. 15, 16).
- 1349 [9] P. Langacker. *The Physics of Heavy Z' Gauge Bosons*. *Rev. Mod. Phys.* **81** (2009),
1350 pp. 1199–1228. arXiv: [0801.1345 \[hep-ph\]](#) (cit. on pp. 16, 17).
- 1351 [10] G. Ferretti and D. Karateev. *Fermionic UV completions of composite Higgs models*.
1352 *Journal of High Energy Physics* **2014**.3 (Mar. 2014). ISSN: 1029-8479 (cit. on p. 17).
- 1353 [11] L. Vecchi. *A dangerous irrelevant UV-completion of the composite Higgs*. *JHEP* **02**
1354 (2017), p. 094. arXiv: [1506.00623 \[hep-ph\]](#) (cit. on p. 17).
- 1355 [12] K. Agashe, A. Delgado, M. J. May, and R. Sundrum. *RS1, custodial isospin and*
1356 *precision tests*. *JHEP* **08** (2003), p. 050. arXiv: [hep-ph/0308036 \[hep-ph\]](#) (cit. on
1357 p. 17).
- 1358 [13] K. Agashe, R. Contino, and A. Pomarol. *The Minimal composite Higgs model*. *Nucl.*
1359 *Phys. B* **719** (2005), pp. 165–187. arXiv: [hep-ph/0412089 \[hep-ph\]](#) (cit. on p. 17).
- 1360 [14] N. Greiner, K. Kong, J.-C. Park, S. C. Park, and J.-C. Winter. *Model-independent*
1361 *production of a top-philic resonance at the LHC*. *Journal of High Energy Physics* **2015**.4
1362 (2015), p. 29. ISSN: 1029-8479 (cit. on pp. 17, 18).
- 1363 [15] J. H. Kim, K. Kong, S. J. Lee, and G. Mohlabeng. *Probing TeV scale top-philic reso-*
1364 *nances with boosted top-tagging at the high luminosity LHC*. *Phys. Rev. D* **94** (3 2016),
1365 p. 035023 (cit. on p. 17).

- 1366 [16] High Luminosity LHC Project Organization. *The HL-LHC project*. URL: <https://hilumilhc.web.cern.ch/content/hl-lhc-project> (visited on 06/11/2025) (cit. on p. 22).
- 1367
- 1368 [17] ATLAS Collaboration. *Standard Model Summary Plots October 2023*. ATL-PHYS-
- 1369 PUB-2023-039. 2023. URL: <https://cds.cern.ch/record/2882448> (cit. on p. 23).
- 1370 [18] ATLAS Collaboration. *Topological cell clustering in the ATLAS calorimeters and its*
- 1371 *performance in LHC Run 1*. Eur. Phys. J. C **77** (2017), p. 490. arXiv: [1603.02934](https://arxiv.org/abs/1603.02934)
- 1372 [hep-ex] (cit. on p. 32).
- 1373 [19] W. Lampl et al. *Calorimeter clustering algorithms: description and performance*. ATL-
- 1374 LARG-PUB-2008-002. 2008. URL: <https://cds.cern.ch/record/1099735> (cit. on p. 32).
- 1375 [20] ATLAS Collaboration. *Performance of the ATLAS track reconstruction algorithms in*
- 1376 *dense environments in LHC Run 2*. Eur. Phys. J. C **77** (2017), p. 673. arXiv: [1704.07983](https://arxiv.org/abs/1704.07983)
- 1377 [hep-ex] (cit. on p. 33).
- 1378 [21] T. Cornelissen et al. *Concepts, design and implementation of the ATLAS New Tracking*
- 1379 (*NEWT*). Tech. rep. Geneva: CERN, 2007. URL: <https://cds.cern.ch/record/1020106>
- 1380 (cit. on p. 33).
- 1381 [22] R. Frühwirth. *Application of Kalman filtering to track and vertex fitting*. Nucl. Instrum.
- 1382 Methods Phys. Res. A **262.2** (1987), pp. 444–450. ISSN: 0168-9002 (cit. on p. 34).
- 1383 [23] T. Cornelissen et al. *The global χ^2 track fitter in ATLAS*. Journal of Physics: Confer-
- 1384 ence Series **119.3** (2008), p. 032013 (cit. on p. 34).
- 1385 [24] ATLAS Collaboration. *Improved electron reconstruction in ATLAS using the Gaussian*
- 1386 *Sum Filter-based model for bremsstrahlung*. ATLAS-CONF-2012-047. 2012. URL: <https://cds.cern.ch/record/1449796> (cit. on p. 34).
- 1387

- 1388 [25] D. Wicke. *A new algorithm for solving tracking ambiguities*. Tech. rep. Oct. 1998. URL:
1389 <https://cds.cern.ch/record/2625731> (cit. on p. 34).
- 1390 [26] A. Salzburger and on behalf of the ATLAS Collaboration. *Optimisation of the ATLAS*
1391 *Track Reconstruction Software for Run-2*. *Journal of Physics: Conference Series* 664.7
1392 (2015), p. 072042 (cit. on p. 34).
- 1393 [27] ATLAS Collaboration. *Measurements of b-jet tagging efficiency with the ATLAS de-*
1394 *tector using $t\bar{t}$ events at $\sqrt{s} = 13 \text{ TeV}$* . *JHEP* 08 (2018), p. 089. arXiv: [1805.01845](https://arxiv.org/abs/1805.01845)
1395 [[hep-ex](#)] (cit. on p. 37).
- 1396 [28] ATLAS Collaboration. *Graph Neural Network Jet Flavour Tagging with the ATLAS*
1397 *Detector*. ATL-PHYS-PUB-2022-027. 2022. URL: <https://cds.cern.ch/record/2811135>
1398 (cit. on p. 38).
- 1399 [29] A. Duperrin. *Flavour tagging with graph neural networks with the ATLAS detector*.
1400 Tech. rep. Presented at DIS2023, Michigan State University, USA. Geneva: CERN,
1401 2023. arXiv: [2306.04415](https://arxiv.org/abs/2306.04415) [[hep-ex](#)]. URL: <https://cds.cern.ch/record/2860610> (cit. on
1402 p. 38).
- 1403 [30] S. Van Stroud et al. *FTAG Run-3 Algorithms Performance*. Tech. rep. Geneva: CERN,
1404 2023. URL: <https://cds.cern.ch/record/2872884> (cit. on p. 38).
- 1405 [31] ATLAS Collaboration. *Electron reconstruction and identification in the ATLAS exper-*
1406 *iment using the 2015 and 2016 LHC proton–proton collision data at $\sqrt{s} = 13 \text{ TeV}$* . *Eur.*
1407 *Phys. J. C* 79 (2019), p. 639. arXiv: [1902.04655](https://arxiv.org/abs/1902.04655) [[physics.ins-det](#)] (cit. on pp. 26,
1408 39, 40, 42).

- 1409 [32] ATLAS Collaboration. *Electron and photon performance measurements with the AT-*
1410 *LAS detector using the 2015–2017 LHC proton–proton collision data*. *JINST* **14** (2019),
1411 P12006. arXiv: [1908.00005 \[hep-ex\]](https://arxiv.org/abs/1908.00005) (cit. on pp. 39, 40, 42).
- 1412 [33] ATLAS Collaboration. *Electron Identification with a Convolutional Neural Network in*
1413 *the ATLAS Experiment*. ATL-PHYS-PUB-2023-001. 2023. URL: <https://cds.cern.ch/record/2850666> (cit. on p. 42).
- 1415 [34] ATLAS Collaboration. *Muon reconstruction and identification efficiency in ATLAS*
1416 *using the full Run 2 pp collision data set at $\sqrt{s} = 13 \text{ TeV}$* . *Eur. Phys. J. C* **81** (2021),
1417 p. 578. arXiv: [2012.00578 \[hep-ex\]](https://arxiv.org/abs/2012.00578) (cit. on pp. 43, 44).
- 1418 [35] ATLAS Collaboration. *Muon reconstruction performance of the ATLAS detector in*
1419 *proton–proton collision data at $\sqrt{s} = 13 \text{ TeV}$* . *Eur. Phys. J. C* **76** (2016), p. 292. arXiv:
1420 [1603.05598 \[hep-ex\]](https://arxiv.org/abs/1603.05598) (cit. on p. 43).
- 1421 [36] ATLAS Collaboration. *Performance of missing transverse momentum reconstruction*
1422 *with the ATLAS detector using proton–proton collisions at $\sqrt{s} = 13 \text{ TeV}$* . *Eur. Phys.*
1423 *J. C* **78** (2018), p. 903. arXiv: [1802.08168 \[hep-ex\]](https://arxiv.org/abs/1802.08168) (cit. on p. 44).
- 1424 [37] ATLAS Collaboration. *E_T^{miss} performance in the ATLAS detector using 2015–2016*
1425 *LHC pp collisions*. ATLAS-CONF-2018-023. 2018. URL: <https://cds.cern.ch/record/2625233> (cit. on p. 45).
- 1427 [38] ATLAS Collaboration. *Observation of electroweak production of two jets in association*
1428 *with an isolated photon and missing transverse momentum, and search for a Higgs*
1429 *boson decaying into invisible particles at 13 TeV with the ATLAS detector*. *Eur. Phys.*
1430 *J. C* **82** (2022), p. 105. arXiv: [2109.00925 \[hep-ex\]](https://arxiv.org/abs/2109.00925) (cit. on p. 46).

- 1431 [39] ATLAS Collaboration. *Analysis of $t\bar{t}H$ and $t\bar{t}W$ production in multilepton final states*
1432 *with the ATLAS detector.* ATLAS-CONF-2019-045. 2019. URL: [https://cds.cern.ch/](https://cds.cern.ch/record/2693930)
1433 record/2693930 (cit. on p. 61).
- 1434 [40] ATLAS Collaboration. *Measurement of the total and differential cross-sections of $t\bar{t}W$*
1435 *production in pp collisions at $\sqrt{s} = 13 \text{ TeV}$ with the ATLAS detector.* JHEP 05 (2024),
1436 p. 131. arXiv: 2401.05299 [hep-ex] (cit. on p. 61).
- 1437 [41] ATLAS Collaboration. *Evidence for $t\bar{t}t\bar{t}$ production in the multilepton final state in*
1438 *proton–proton collisions at $\sqrt{s} = 13 \text{ TeV}$ with the ATLAS detector.* Eur. Phys. J. C 80
1439 (2020), p. 1085. arXiv: 2007.14858 [hep-ex] (cit. on p. 61).
- 1440 [42] ATLAS Collaboration. *Observation of four-top-quark production in the multilepton*
1441 *final state with the ATLAS detector.* Eur. Phys. J. C 83 (2023), p. 496. arXiv: 2303.
1442 15061 [hep-ex] (cit. on p. 61).
- 1443 [43] ATLAS Collaboration. *Search for R -parity-violating supersymmetry in a final state*
1444 *containing leptons and many jets with the ATLAS experiment using $\sqrt{s} = 13 \text{ TeV}$*
1445 *proton–proton collision data.* Eur. Phys. J. C 81 (2021), p. 1023. arXiv: 2106.09609
1446 [hep-ex] (cit. on p. 61).
- 1447 [44] E. Gerwick, T. Plehn, S. Schumann, and P. Schichtel. *Scaling Patterns for QCD Jets.*
1448 JHEP 10 (2012), p. 162. arXiv: 1208.3676 [hep-ph] (cit. on pp. 61, 62).